Journal of Geophysical Research: Atmospheres

RESEARCH ARTICLE
10.1029/2018JD029046

Methyl, Ethyl, and Propyl Nitrates: Global Distribution and Impacts on Reactive Nitrogen in Remote Marine Environments

Jenny A. Fisher[1,2], Elliot L. Atlas[3], Barbara Barletta[4], Simone Meinardi[4], Donald R. Blake[4], Chelsea R. Thompson[5,6], Thomas B. Ryerson[6], Jeff Peischl[5,6], Zitely A. Tzompa-Sosa[7], and Lee T. Murray[8]

[1]Centre for Atmospheric Chemistry, School of Chemistry, University of Wollongong, Wollongong, New South Wales, Australia, [2]School of Earth and Environmental Sciences, University of Wollongong, Wollongong, New South Wales, Australia, [3]Department of Atmospheric Sciences, Rosenstiel School of Marine and Atmospheric Sciences, University of Miami, Miami, FL, USA, [4]Department of Chemistry, University of California, Irvine, CA, USA, [5]Cooperative Institute for Research in Environmental Sciences, University of Colorado Boulder, Boulder, CO, USA, [6]Chemical Sciences Division, NOAA Earth System Research Laboratory, Boulder, CO, USA, [7]Department of Atmospheric Science, Colorado State University, Fort Collins, CO, USA, [8]Department of Earth and Environmental Sciences, University of Rochester, Rochester, NY, USA

Key Points:
- Model including air-sea exchange reproduces observed alkyl nitrates from 20 years of airborne data
- Methyl nitrate is the dominant form of reactive nitrogen in the tropical Pacific and Southern Ocean
- Alkyl nitrates serve as a small but growing source of nitrogen oxides to the remote troposphere

Supporting Information:
- Supporting Information S1

Correspondence to:
J. A. Fisher,
jennyf@uow.edu.au

Citation:
Fisher, J. A., Atlas, E. L., Barletta, B., Meinardi, S., Blake, D. R., Thompson, C., et al. (2018). Methyl, ethyl, and propyl nitrates: Global distribution and impacts on reactive nitrogen in remote marine environments. *Journal of Geophysical Research: Atmospheres*, *123*, 12,429–12,451. https://doi.org/10.1029/2018JD029046

Received 22 MAY 2018
Accepted 14 SEP 2018
Accepted article online 18 SEP 2018
Published online 9 NOV 2018

Abstract Alkyl nitrates ($RONO_2$) are important components of tropospheric reactive nitrogen that serve as reservoirs for nitrogen oxides ($NO_x \equiv NO + NO_2$). Here we implement a new simulation of atmospheric methyl, ethyl, and propyl nitrate chemistry in a global chemical transport model (GEOS-Chem). We show that the model can reproduce the spatial and seasonal variability seen in a 20-year ensemble of airborne observations. Methyl nitrate accounts for 17 Gg N globally, with maxima over the tropical Pacific and Southern Ocean. Propyl nitrate is enhanced in continental boundary layers, but its global impact (6 Gg N) is limited by a short lifetime (8 days vs. 26 days for methyl nitrate and 14 days for ethyl nitrate) that inhibits long-range transport. Ethyl nitrate has the smallest impact of the three species (4 Gg N). We find that methyl nitrate is the dominant form of reactive nitrogen (NO_y) in the Southern Ocean marine boundary layer, where its addition to the model corrects a large NO_y underestimate in austral winter relative to recent aircraft data. $RONO_2$ serve as a small net NO_x source to the marine troposphere, except in the northern midlatitudes where the continental outflow is enriched in precursors that promote NO_x loss via $RONO_2$ formation. Recent growth in NO_x emissions from East Asia has enhanced the role of $RONO_2$ as a source of NO_x to the remote free troposphere. This relationship implies projected future NO_x emissions growth across the southern hemisphere may further enhance the importance of $RONO_2$ as a NO_x reservoir.

Plain Language Summary Nitrogen in the atmosphere has many impacts on atmospheric chemistry, including affecting how polluted the air is. Many nitrogen-containing gases are released over polluted areas and are quickly broken down—staying far away from remote areas like the ocean. In this paper, we investigate a group of nitrogen gases (called *alkyl nitrates*) that break down more slowly and so stay in the atmosphere long enough to be transported to the otherwise pollution-free remote Pacific Ocean. These gases are also created naturally in the ocean and then make their way into the atmosphere, changing the atmospheric chemistry over the ocean. We use 20 years of measurements collected from aircraft, combined with a computer model, to determine the abundance and impacts of alkyl nitrates. We find that the smallest alkyl nitrates are particularly important over the Southern Ocean, where there are few other sources of nitrogen. We show that alkyl nitrates are playing an increasingly important role over the remote oceans because of recent growth in East Asian air pollution. This relationship implies that these gases may have a stronger influence on atmospheric chemistry over remote ocean areas in future if anticipated pollution growth in Africa, South America, and Southeast Asia is realised.

1. Introduction

Nitrogen oxides ($NO_x \equiv NO + NO_2$) are precursors to tropospheric ozone production, contribute to inorganic and organic aerosol formation, and enhance nitrogen deposition to ecosystems. Atmospheric NO_x has a short lifetime (typically <12 hr; Liu et al., 2016; Romer et al., 2016; Valin et al., 2013) but can be sequestered via formation of longer-lived reactive nitrogen reservoir species including peroxyacyl nitrates (PANs) and alkyl nitrates

($RONO_2$). In remote environments where primary NO_x emissions are limited, degradation of these nitrogen reservoirs serves as the dominant NO_x source. While NO_x production from PANs requires warm temperatures and is most significant in subsiding polluted air masses (Hudman et al., 2004; Singh, 1987; Zhang et al., 2008), the source from $RONO_2$ is primarily due to photolysis (Clemitshaw et al., 1997; Talukdar et al., 1997) and is therefore more diffuse. In this work, we focus exclusively on short-chain (C_1–C_3) $RONO_2$, which have lifetimes that are sufficiently long to allow long-range transport from source regions. Short-chain $RONO_2$ species have both continental (Farmer et al., 2011; Perring et al., 2010; Roberts et al., 1996) and marine (Chuck, 2002; Dahl et al., 2005) sources and have been observed in diverse environments across the globe (Atlas et al., 1993; Blake et al., 1999; Blake et al., 2003; Talbot et al., 2000). These $RONO_2$ species may therefore provide a potentially significant NO_x source to regions of the remote troposphere where decomposition of PANs is limited. Here we use airborne observations collected during 19 aircraft campaigns over a 20-year period from 1996 to 2017 as constraints to develop a new simulation of methyl, ethyl, and propyl $RONO_2$ in a chemical transport model (GEOS-Chem), including a new mechanistic treatment of their ocean source. We then use the model to quantify their global distribution and the implications for reactive nitrogen in remote marine regions.

Alkyl nitrate formation in the atmosphere begins with oxidation of a parent volatile organic compound (VOC, denoted RH in reaction (1)—here methane (CH_4), ethane (C_2H_6), or propane (C_3H_8)—by the hydroxyl radical (OH) in the presence of oxygen to form a peroxy radical ($RO_2^{\cdot}$):

$$RH + OH \rightarrow R^{\cdot} + H_2O \quad (1)$$

$$R^{\cdot} + O_2 \rightarrow RO_2^{\cdot} \quad (2)$$

In the presence of NO_x, the RO_2 radical reacts with NO to either convert NO to NO_2 ((R3), the dominant pathway) or form an alkyl nitrate ((R4)):

$$RO_2^{\cdot} + NO \rightarrow RO^{\cdot} + NO_2 \quad (3)$$

$$RO_2^{\cdot} + NO \rightarrow RONO_2 \quad (4)$$

In highly polluted urban environments, methyl nitrate can also be formed via $RO^{\cdot} + NO_2$, but this source is thought to be insignificant on the global scale (Flocke et al., 1998). The branching ratio between reactions 4 and 3 (combined where relevant with the branching ratio for formation of the specific $RO_2^{\cdot}$ isomer) represents the yield of $RONO_2$, referred to as α. For the species considered here, α increases from <1% for methyl nitrate (CH_3ONO_2; Flocke et al., 1998) to ≈2% for ethyl nitrate ($C_2H_5ONO_2$; Ranschaert et al., 2000) to >3% for propyl nitrate ($C_3H_7ONO_2$; Atkinson et al., 1982)—although precise measurement of α remains an important source of uncertainty in atmospheric $RONO_2$ budgets (Butkovskaya et al., 2009; 2012; Khan et al., 2015; Nault et al., 2016; Williams et al., 2014). While reaction 3 has no net impact on available atmospheric NO_x, reaction 4 can recycle NO_x, temporarily sequester NO_x, or permanently remove NO_x from the atmosphere, depending on the lifetime and fate of the $RONO_2$ produced (Fisher et al., 2016; Perring et al., 2013). Short-chain $RONO_2$ are removed primarily by photolysis followed by OH-initiated oxidation (Clemitshaw et al., 1997; Talukdar et al., 1997)—both of which return NO_2 to the atmospheric NO_x pool.

Observations of elevated short-chain $RONO_2$ (particularly methyl nitrate) concentrations in the marine boundary layer, along with supersaturated ocean surface waters, suggest a direct $RONO_2$ source from seawater (Atlas et al., 1993; Blake et al., 1999; Blake et al., 2003; Chuck, 2002; Dahl et al., 2005; Talbot et al., 2000). Ocean emission is expected to be an especially significant source of methyl nitrate (Neu et al., 2008), given the low methyl nitrate yield from in situ photochemical formation (Flocke et al., 1998). In situ $RONO_2$ production in seawater can occur via photochemical (Dahl et al., 2007; Dahl & Saltzman, 2008) and biological (M. J. Kim et al., 2015) processes, leading to supersaturation that drives a net $RONO_2$ flux from the ocean to the atmosphere (Chuck, 2002; Dahl et al., 2005). Although this flux has not been measured directly, it is consistent with observations showing elevated $RONO_2$ in surface waters (Chuck, 2002; Dahl et al., 2005; Hughes et al., 2008) and in the marine boundary layer (Atlas et al., 1993; Blake et al., 2003; Jones et al., 1999; Talbot et al., 2000) over the tropics and the South Pacific.

To date, there has been only one attempt to construct a distribution of the ocean $RONO_2$ flux for use in global models. Using aircraft observations from the PEM-Tropics campaigns, Neu et al. (2008) inferred a constant ocean flux of 0.35 Tg N yr^{-1}, mainly from the tropical Pacific with a small contribution from the Southern

Ocean. However, the model used in their study did not include atmospheric production of $RONO_2$ via reactions (1)–(4), which likely exaggerated the size of the ocean source (Williams et al., 2014). The Neu et al. (2008) estimate was also hampered by the limitations of the aircraft data available at the time, including a lack of seasonal information and particularly large uncertainties for the Southern Ocean, where only one flight leg crossed south of 45°S. Despite these limitations, this estimate is the only one to have been used in global modeling studies of $RONO_2$ and their impacts.

Over the past two decades, a large global data set of airborne C_1-C_3 $RONO_2$ observations has been amassed, spanning a diverse range of environments, latitudes, and seasons. Although observations suggest that short-chain $RONO_2$ may be the dominant form of reactive nitrogen in remote marine environments (Jones et al., 1999; Talbot et al., 2000), many models ignore these species completely. The few global models that have attempted to simulate short-chain $RONO_2$ struggle to reproduce the ensemble of observations using a single set of model assumptions (Williams et al., 2014; Khan et al., 2015), with uncertainty in the ocean source a large contributor (Williams et al., 2014). For example, two global models both using the top-down ocean flux derived by Neu et al. (2008) show estimates of the ocean contribution to the total methyl nitrate burden that range from as little as 15% (Khan et al., 2015) to as much as 68% (Williams et al., 2014).

Here we develop a new simulation for C_1-C_3 $RONO_2$ in the global GEOS-Chem chemical transport model, which has been widely used for studies of reactive nitrogen (e.g., Fischer et al., 2014; Geddes & Martin, 2017; Paulot et al., 2013; Walker et al., 2010) and ozone budgets (e.g., Hu et al., 2017; Wu et al., 2007; Zhang et al., 2010) but has previously neglected these smaller alkyl nitrates. Our model includes a new, bottom-up estimate of ocean $RONO_2$ emissions that is independent of the top-down estimate from Neu et al. (2008) used in previous models (section 2). We exploit the 20-year ensemble of global airborne data to evaluate the model. Of particular value are the recent HIPPO and Atmospheric Tomography (ATom) observations that span the entire Pacific Ocean over a range of seasons. After showing that the new simulation can reproduce the general features of the observations (section 3), we use it to evaluate the impact of short-chain $RONO_2$ on global distributions of reactive nitrogen and ozone (section 4). We then quantify the role of exported $RONO_2$ formed near major NO_x source regions on the NO_x budget in remote regions (section 5). Finally, we test the sensitivity of our results to recent changes in the global distribution of NO_x and VOC emissions (section 6).

2. Model Description

We use as base model a modified version of GEOS-Chem v9-02 with updates that have been described in detail by P. S. Kim et al. (2015), Fisher et al. (2016), Travis et al. (2016), and Marais et al. (2016). Fisher et al. (2016) made a number of improvements to simulation of $\geq C_4$ $RONO_2$ but did not include C_1-C_3 $RONO_2$, which are added here for the first time. We simulate 2013 (plus a 2-month spin-up) driven by assimilated meteorology from the Global Monitoring and Assimilation Office Goddard Earth Observing System (GEOS-FP) product. The native 0.25° × 0.3125° resolution of GEOS-FP is downgraded to 2° × 2.5° for the global simulation used here. Sensitivity simulations described below use the coarser 4° × 5° resolution for expediency, and we find there are no major differences in the global simulation between the two resolutions. We use a vertical resolution of 47 levels from the surface to 0.01 hPa, with some native GEOS-FP levels lumped in the stratosphere.

We include four new $RONO_2$ species: methyl nitrate (CH_3ONO_2, referred to here as $MeNO_3$), ethyl nitrate ($C_2H_5ONO_2$, referred to here as $EtNO_3$), and n-propyl and isopropyl nitrates ($C_3H_7ONO_2$, referred to here as n-$PrNO_3$ and i-$PrNO_3$, respectively, or their sum $PrNO_3$). Treatment of these species is detailed in the following subsections.

2.1. Ocean $RONO_2$ Flux

Measurements of enhanced $RONO_2$ in the marine boundary layer suggest an ocean source in both the tropics (Atlas et al., 1993; Blake et al., 2003) and the high southern latitudes (Blake et al., 1999; Fischer et al., 2002; Jones et al., 1999). In the tropics, this source has been confirmed by coincident atmospheric and seawater measurements showing high $MeNO_3$ and $EtNO_3$ supersaturation anomalies in both the Atlantic (Chuck, 2002) and Pacific (Dahl et al., 2005). The origin of the atmospheric enhancement over the Southern Ocean is less clear, with a small shipborne data set showing tightly coupled atmosphere and ocean concentrations but only occasional supersaturation (Hughes et al., 2008).

The mechanism for oceanic $RONO_2$ formation remains uncertain. Experimental evidence points to aqueous phase reaction between photochemically produced NO and RO_2 radicals as a likely $RONO_2$ source in surface

waters (Dahl et al., 2003; Moore & Blough, 2002). Seawater $RONO_2$ production is generally limited by available nitrite (Dahl & Saltzman, 2008), which photolyzes to produce NO radicals (Anifowose & Sakugawa, 2017; Olasehinde et al., 2010; Zafiriou & McFarland, 1981). In dark environments (e.g., at depth) heterotrophic bacteria can provide an additional $RONO_2$ source, potentially via production of NO radicals (M. J. Kim et al., 2015).

Few seawater observations are available to constrain the global distribution of $RONO_2$ in the ocean. Representing the ocean-atmosphere flux of $RONO_2$ in global atmospheric models is therefore a challenge. Neu et al. (2008) calculated the flux using a single average Pacific Ocean value for the concentration gradient across the ocean-atmosphere interface, which they then scaled to fit aircraft observations over the tropics (10°S to 10°N) and Southern Ocean (south of 45°S). Neither seasonal variability nor spatial variability within each basin were accounted for, and emissions outside these regions were assumed to be negligible. More recent simulations (Khan et al., 2015; Williams et al., 2014) have simply applied variants of the Neu et al. (2008) fluxes as an oceanic emission.

Here we instead apply a mechanistic treatment of bidirectional $RONO_2$ air-sea exchange that couples the flux to sea surface $MeNO_3$ and $EtNO_3$ concentrations and includes seasonal and spatial variability driven by dynamic changes in wind speed, sea surface temperature, and nitrite availability. We find from a model sensitivity simulation that the ocean $PrNO_3$ flux is too small to significantly impact the atmospheric simulation and do not include it here. We define ocean concentrations of $MeNO_3$ and $EtNO_3$ as described below. Air-sea exchange then follows Johnson (2010) with updated Henry's Law coefficients from the Sander (2015) compilation. The air-sea exchange parameterization depends on both sea surface temperature and wind speed, which vary with the spatial (2° × 2.5°) and temporal (hourly) resolution of the input GEOS-FP meteorology. While we do not explore interannual variability in $RONO_2$ air-sea exchange in this work, our parameterization would enable future studies of this nature (e.g., the impact of the El Niño-Southern Oscillation on air-sea exchange through changes in wind speed and temperature).

Seawater $RONO_2$ measurements are too rare to define a global distribution. Instead, we link seawater concentrations to nitrite distributions. Lab and field experiments in the tropical Pacific and along the east coast of the United States have shown that NO derived from nitrite is generally the limiting factor for ocean $RONO_2$ production (Dahl & Saltzman, 2008; Dahl et al., 2012). We identify broad spatial regimes with nonzero sea surface nitrite using observations from four data sets: the Repeat Hydrography Cruises coordinated by National Oceanographic and Atmospheric Administration through the U.S. Global Ocean Carbon and Repeat Hydrography Program (available from https://cchdo.ucsd.edu/search?q=USHYDRO), the Geochemical Ocean Sections Study v2 Hydrographic and Tracer Data (available via Ocean Data View, https://odv.awi.de/data/ocean/geosecs/), a data set compiled by J. L. Reid and A. W. Mantyla (available via Ocean Data View, https://odv.awi.de/data/ocean/reid-mantyla/), and the Global Ocean Data Analysis Project version 2 (Olsen et al., 2016). The measurements are relatively sparse, but comparing the data sets shows that nonzero nitrite is generally found in the southern high latitudes (south of 40°S), in the northern high latitudes (north of 40°N in the Pacific and north of 50°N in the Atlantic), and in the tropics (from 15°S to 10°N). We consider these as regions where there is sufficient nitrite to make $RONO_2$ production possible.

In these regions with nonzero nitrite, we set fixed seawater $RONO_2$ concentrations as described below; elsewhere, the ocean is a sink for $MeNO_3$ and $EtNO_3$. Drivers of site-to-site variability are poorly understood, and so we apply a single ocean $MeNO_3$ concentration in each region (southern high latitudes, northern high latitudes, and tropics), based where possible on seawater measurements. We then set fixed $EtNO_3$ concentrations using an assumed 6:1 ratio of ocean $MeNO_3$:$EtNO_3$ (Dahl et al., 2007). As $MeNO_3$ has not been measured in the northern high latitudes, we originally applied the same concentration value in the northern and southern high latitudes but found this led to large biases relative to the aircraft data in the North Pacific. Our final seawater $MeNO_3$ concentrations are 200 pM in the southern high latitudes (upper limit from Hughes et al., 2008) and 120 pM in the northern high latitudes (chosen to fit the atmospheric observations).

In the tropics, Dahl et al. (2007) showed that $RONO_2$-enriched waters also have elevated chlorophyll, a relationship that is attributed to covariation between chlorophyll and nitrite availability (rather than direct $RONO_2$ production by phytoplankton). Satellite-derived chlorophyll provides seasonally and spatially resolved information that is not available via the in situ nitrite data sets. We therefore further refine our tropical $RONO_2$ source using MODIS monthly mean chlorophyll *a* concentrations from the year 2003, assuming seawater

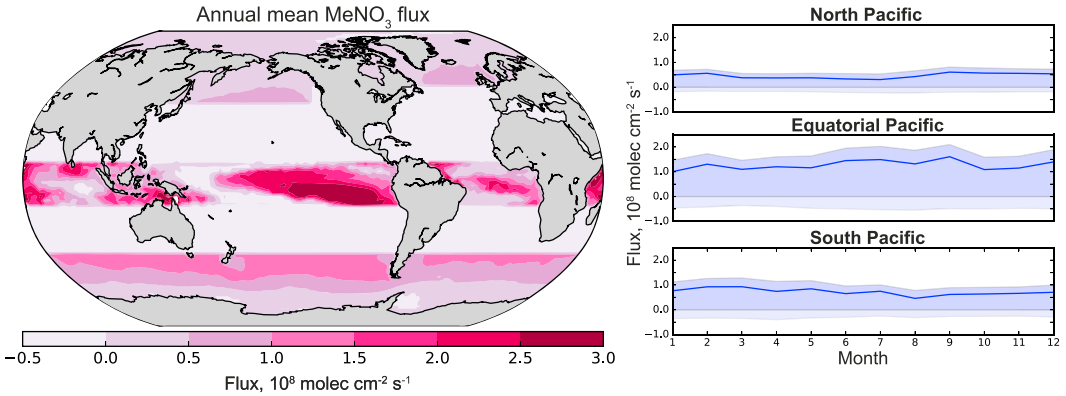

Figure 1. Net ocean-to-atmosphere flux of methyl nitrate ($MeNO_3$) in GEOS-Chem. (left) Annual mean flux for all ocean grid squares. (right) Seasonal cycle of the net (solid line), upward (dark shading), and downward (light shading) flux in the North Pacific (130–180°W, 40–60°N), Equatorial Pacific (130–180°W, 15°S – 10°N), and South Pacific (130–180°W, 40–70°S).

$MeNO_3$ concentrations of 400 pM (upper limit from Dahl et al., 2007) when chlorophyll >0.1 mg/m^3 and 25 pM otherwise (low-chlorophyll Warm Pool measurements from Dahl et al., 2007). We apply the chlorophyll-based cutoff only in the tropics, where the empirical relationship has been observed. We find that including this chlorophyll-derived proxy improves simulation of $RONO_2$ in the tropical marine boundary layer relative to a version that allowed $RONO_2$ production in all tropical waters. Our parameterization does not take into account interannual variability in either nitrite or chlorophyll, which could be significant in the tropics (e.g., during different phases of the El Niño-Southern Oscillation). Nonetheless, our parameterization captures the large-scale features of the atmospheric observations collected over multiple years (section 3).

Figure 1 shows the simulated annual mean net ocean-atmosphere $MeNO_3$ flux; the $EtNO_3$ flux shows the same pattern but with lower values. As seen in the figure, on an annual timescale the net flux is positive in the tropics and high latitudes, consistent with observations of an oceanic source to the atmosphere. Elsewhere (i.e., in regions assumed incompatible with seawater $RONO_2$ production), the ocean is always a small net sink. Spatial variability across the tropics comes from the chlorophyll-based constraint. In all regions, the flux varies seasonally with changes in wind speed and sea surface temperature (right panels of Figure 1).

2.2. Chemistry

Chemical production of $RONO_2$ occurs via reaction of a VOC-derived peroxy radical ($RO_2^{\cdot}$) with NO (reactions (1)-(4). We do not consider $RONO_2$ from $RO^{\cdot}+NO_2$ reaction in fire plumes (Simpson et al., 2002), as this source contributes less than 2% of the global $RONO_2$ budget (Khan et al., 2015; Williams et al., 2014). We assume the dominant sources of the methyl, ethyl, and propyl $RO_2^{\cdot}$ radicals are reactions (1)–(2) (i.e., oxidation of methane, ethane, and propane, respectively). These $RO_2^{\cdot}$ radicals can also be produced during degradation of larger VOCs (including alkanes, aldehydes, and ketones) that are lumped in the GEOS-Chem mechanism. Standard treatment of the $RO_2^{\cdot}$ produced from degradation of lumped species in GEOS-Chem has historically been different for alkanes than for aldehydes and ketones. For species derived from lumped alkanes, the mechanism assumes an $RO_2^{\cdot}$ distribution of 50% (by carbon) ethyl peroxy, 40% isopropyl peroxy, and 10% n-propyl peroxy. Other lumped species produce only ethyl peroxy, based on the assumption that higher aldehydes react like propanal and higher ketones like methyl ethyl ketone (Horowitz et al., 1998).

We find that this configuration overestimates $EtNO_3$ by a factor of 3–4 in both near-source and remote regions and underestimates $PrNO_3$ by a factor of 2 in source regions. Tracing the exact composition of the $RO_2^{\cdot}$ radical pool would require specifying the fraction of lumped species that come from each component VOC — information that we do not have. Instead, we find that we can reproduce observed $EtNO_3$ to first order across a range of environments by removing the ethyl peroxy source from lumped species. To avoid adverse effects on other model species, we replace model ethyl peroxy from higher VOC degradation with a generic $RO_2^{\cdot}$ radical that behaves like ethyl peroxy but does not form $EtNO_3$. Moreover, we assume that the degradation of the aldehydes and ketones produces 40% isopropyl peroxy and 10% n-propyl peroxy, analogous to

the alkane degradation. This greatly improves the simulation of $PrNO_3$. The remaining 50% then forms the generic $RO_2^{\cdot}$ radical that behaves like ethyl peroxy but does not from $EtNO_3$.

The $RONO_2$ yield from reaction (4) (i.e., the branching ratio between (R4) and (R3)) is referred to as α and is a source of ongoing uncertainty in the $RONO_2$ budget, despite decades of experimental and computational study (Dibble, 2008). For higher ($\geq C_2$) alkanes, $RONO_2$ production increases significantly with temperature (Lee et al., 2014; Nault et al., 2016). Here we use empirically derived $RONO_2$ yields that depend on temperature, pressure, and carbon number (Carter & Atkinson, 1989). For methyl nitrate, Butkovskaya et al. (2012) measured the branching ratios at pressures representative of the upper troposphere and extrapolated these to the rest of the troposphere, resulting in a tropospheric-mean branching ratio of $\alpha = 1.0 \pm 0.7 \cdot 10^{-2}$. This value is roughly 2 orders of magnitude larger than previously derived by Flocke et al. (1998), who extrapolated results from a box model constrained by airborne measurements to derive a tropospheric branching ratio of $\alpha = 1.5-3.0 \cdot 10^{-4}$. Williams et al. (2014) tested both the Flocke et al. (1998) and Butkovskaya et al. (2012) yields and found the latter overestimated methyl nitrate observations by an order of magnitude. We similarly found that the Butkovskaya et al. (2012) yield led to a significant overestimate of $MeNO_3$ in GEOS-Chem. For this reason, we use a yield of $\alpha = 3.0 \cdot 10^{-4}$, the upper limit from Flocke et al. (1998).

Alkyl nitrates are predominantly removed by photolysis, followed by OH oxidation (Clemitshaw et al., 1997; Talukdar et al., 1997). We use the Master Chemical Mechanism version 3.3.1 to determine the products (mapped to GEOS-Chem species), with rate constants for OH oxidation from the Jet Propulsion Laboratory Data Evaluation v15-10. Photolysis rates are calculated using the Fast-JX code (Bian & Prather, 2002) with cloud treatment following Liu et al. (2006) as implemented by Mao et al. (2010), with photolysis cross sections from the MPI-Mainz UV/VIS Spectral Atlas (http://satellite.mpic.de/spectral_atlas/cross_sections/) and NO_2 quantum yields of unity for all $RONO_2$ (Higgins et al., 2014). The full mechanism is given in Table S1 in the supporting information.

Deposition is expected to be a minor sink for short-chain $RONO_2$ because of their very low solubility (Perring et al., 2013). However, observations suggest dry deposition can be an important sink for $MeNO_3$ in some environments (Russo et al., 2010). We include here a small dry deposition sink for all $RONO_2$, using the standard resistance-in-series scheme of Wesely (1989) with an assumed reactivity factor equivalent to that of NO_2 ($f_0 = 0.1$). Deposition to the ocean is included in our bidirectional ocean flux parameterization, described in section 2.1.

2.3. Emissions

$RONO_2$ formation via reactions (1)–(4) requires both NO_x and precursor VOCs. For NO_x emissions, we use the configuration described in detail by Travis et al. (2016). Briefly, fossil fuel NO_x comes from the Emission Database for Global Atmospheric Research global inventory (Olivier & Berdowski, 2001), overwritten regionally with EMEP for Europe (Vestreng & Klein, 2002), (Q. Zhang et al., 2009) for Asia (increased by 25% based on satellite NO_2), NPRI for Canada (http://www.ec. gc.ca/inrp-npri/), BRAVO for Mexico (Kuhns et al., 2005), and NEI2011 for the United States (with modifications described by Travis et al., 2016). Aircraft emissions are from the AEIC inventory (Stettler et al., 2011). Additional NO_x emissions come from the Quick Fire Emissions Database (QFED) (Darmenov & Da Silva, 2013) for biomass burning, Hudman et al. (2012) for soil and fertiliser, and Murray et al. (2012) for lightning.

Methane, ethane, and propane are the dominant VOC precursors to C_1-C_3 $RONO_2$ production (see section 2.2 for a discussion of other sources). We prescribe methane surface concentrations based on spatially kriged monthly mean flask observations collected by the National Oceanographic and Atmospheric Administration Global Monitoring Division (Murray, 2016). Above the surface layer, methane is treated as a standard model species subject to advection and chemistry.

Anthropogenic ethane and propane emissions are shown in Figure S1. We apply ethane emissions from the 2010 emission inventory from Tzompa-Sosa et al. (2017), obtained by combining scaled global estimates from a satellite methane inversion (Turner et al., 2015) with the 2011 National Emissions Inventory (NEI) (NEI2011) over the United States. Tzompa-Sosa et al. (2017) showed that ethane distributions simulated using these emissions capture the seasonal and spatial distributions seen in surface and aircraft observations from around the world. $RONO_2$ sensitivity to recent changes in ethane emissions driven by oil and gas extraction (Dalsøren et al., 2018; Helmig et al., 2014; Helmig et al., 2016) is discussed in section 6.

Table 1
Global Mean Burdens, Lifetimes, and Source/Sink Terms for C_1-C_3 Alkyl Nitrates in GEOS-Chem

	Methyl nitrate	Ethyl nitrate	Propyl nitrate
Burden (Gg N)	17	3.7	5.8
Lifetime (days)	26	14	8.3
Sources (Gg N a^{-1})			
Chemical production	81	66	254
Ocean emission	157	27	n/a
Sinks (Gg N a^{-1})			
Chemical loss[a]	165	76	221
Ocean uptake	58	11	n/a
Dry deposition	19	7	34

[a]Chemical loss includes both photodissociation and OH oxidation, which cannot be separated in the model diagnostics.

Propane emissions are calculated following the same methodology as for ethane (Tzompa-Sosa et al., 2017). Globally, base emissions are scaled to the methane emissions of Turner et al. (2015) assuming a propane/methane mass ratio of 0.0663 kg/kg for biofuels (Akagi et al., 2011) and 0.0932 kg/kg for oil and gas (based on emission ratios from Katzenstein et al., 2003, combined with enhancement ratios from Kang et al., 2014). Tzompa-Sosa et al. (2017) previously showed that the Turner et al. (2015) emissions do not show a similar spatial distribution to known U.S. oil and gas wells. To match the oil and gas distribution over the United States, we use the NEI2011 inventory with the assumption that propane represents 3% of the lumped alkane species (Simon et al., 2010; Yarwood et al., 2005). The resulting emissions yield simulated propane concentrations that are much too low relative to airborne propane observations collected near oil and gas sources (FRAPPE, 2014) and downwind (SEAC4RS, 2013). We find that to achieve good agreement with airborne propane observations, we need to scale the NEI2011 inventory by a factor of 10. This large correction is consistent with recent work by Dalsøren et al. (2018), who found that simulated propane was roughly 2–5 times too low near U.S. oil and gas sources even after increasing propane emissions by a factor of 3. Our final simulations use the scaled Turner et al. (2015) emissions globally, overwritten over the United States with NEI2011 emissions scaled by a factor of 10.

3. Global Distribution of C_1-C_3 Alkyl Nitrates

The simulated global mean burdens, lifetimes, and budget terms for C_1-C_3 $RONO_2$ are given in Table 1. On a global scale, $MeNO_3$ is 80% more abundant than $EtNO_3$ and $PrNO_3$ combined. Lifetimes range from 8 days for $PrNO_3$ to 14 days for $EtNO_3$ to 26 days for $MeNO_3$, within the large range estimated by previous studies (Clemitshaw et al., 1997; Khan et al., 2015; Roberts & Fajer, 1989; Talukdar et al., 1997; Williams et al., 2014). The table highlights the importance of ocean exchange, which is responsible for two thirds of the $MeNO_3$ source and one third of the $EtNO_3$ source. Roughly 40% of the $RONO_2$ emitted by the ocean is subsequently lost to ocean uptake, close to an earlier estimate for $MeNO_3$ (Williams et al., 2014; note ocean uptake was included with dry deposition in that work). Nonetheless, chemical loss (including both photolysis and OH oxidation) is the main sink for all three species.

We evaluate the new $RONO_2$ simulation using a large data set of airborne observations collected between 1996 and 2017. Names, dates, and locations of the campaigns are provided in Table 2. The campaigns were largely concentrated over the Pacific and North America, with seasonal coverage spanning all months except December. During the campaigns, whole air samples were collected in stainless steel canisters and analyzed after the flights in off-site laboratories (for measurement details, see Atlas & UCAR/NCAR-Earth Observing Laboratory, 2009; Colman et al., 2001). Observations from pre-2008 aircraft campaigns have been scaled to account for changes to calibration, with scaling factors of 2.13 for $MeNO_3$, 1.81 for $EtNO_3$, and 1.24 for $PrNO_3$ (Simpson et al., 2011).

Figures 2–4 show the annual mean distributions of methyl, ethyl, and propyl nitrates over three altitude bands as simulated by GEOS-Chem (with updated chemistry and emissions as described in section 2), with airborne

Table 2
Aircraft Campaigns Used to Evaluate the GEOS-Chem Short-Chain Alkyl Nitrate Simulation, Ordered by Month

Campaign	Month	Year	Region	Regional Bounds[a]
HIPPO-1[b]	January	2009	Pacific	70°S–60°N, 150°E–100°W[c]
ORCAS	January–February	2016	Southern Ocean	75°S–55°S, 91°W–52°W
ATOM-2	February	2017	Pacific	70°S–60°N, 180°W–130°W[d]
			Atlantic	70°S–60°N, 60°W–0°E[e]
TOPSE	February–May	2000	North American Arctic	60°N–90°N, 104°W–54°W
HIPPO-3[b]	March–April	2010	Pacific	70°S–60°N, 150°E–100°W[c]
TRACE-P	March–April	2001	North Pacific	12°N–46°N, 120°E–120°W
PEM-Tropics B	March–April	1999	Tropical Pacific	35°S–35°N, 155°E–90°W
ARCTAS-A	April	2008	North American Arctic	60°N–90°N, 175°W–50°W
INTEX-B	April–May	2006	North Pacific	19°N–60°N, 175°E–105°W[f]
ITCT-2K2	April–May	2002	North Pacific	26°N–48°N, 130°W–90°W
DC3	May–June	2012	Continental United States	30°N–42°N, 105°W–80°W
HIPPO-4[b]	June–July	2010	Pacific	70°S–60°N, 150°E–100°W[c]
FRAPPE	July–August	2014	Continental United States	37°N–42°N, 110°W–100°W
ATOM-1	August	2016	Pacific	70°S–60°N, 180°W–130°W[d]
			Atlantic	70°S–60°N, 60°W–0°E[e]
SEAC4RS	August–September	2013	Continental United States	19°N–55°N, 130°W–75°W
HIPPO-5[b]	August–September	2011	Pacific	70°S–60°N, 150°E–100°W[c]
TEXAQS	September–October	2006	Continental United States	28°N–35°N, 100°W–93°W
PEM-Tropics A	September–October	1996	Pacific	70°S–35°N, 150°E–125°W[g]
HIPPO-2[b]	October–November	2009	Pacific	70°S–60°N, 150°E–100°W[c]

Note. FRAPPE = Front Range Air Pollution and Photochemistry Experiment; HIPPO = HIAPER Pole-to-Pole Observations; INTEX = Intercontinental Chemical Transport Experiment; ITCT = Intercontinental Transport and Chemical Transformation; ORCAS = O_2/N_2 Ratio and CO_2 Airborne Southern Ocean Study; PEM-Tropics = Pacific Exploratory Mission-Tropics; SEAC4RS = Studies of Emissions and Atmospheric Composition, Clouds, and Climate Coupling by Regional Surveys; TEXAQS = Texas Air Quality Study; TOPSE = Tropospheric Ozone Production about the Spring Equinox; TRACE-P = TRAnsport and Chemical Evolution over the Pacific.
[a]Latitude and longitude bounds of each campaign used to create the model vertical profiles shown in Figures S3, S4, and S5. For all other comparisons, all available aircraft observations are included and averaged to a horizontal resolution of 4° × 5°. [b]Due to data sparsity, the 5 HIPPO campaigns are averaged for calculation of vertical profiles. [c]HIPPO vertical profiles are separated into North Pacific (35°N–60°N, 180°W–130°W), Central Pacific (35°S–35°N, 150°E–120°W), and South Pacific (70°S–35°S, 150°E–100°W). [d] ATom vertical profiles are separated into North Pacific (35°N–60°N, 180°W–130°W), Central Pacific (35°S–35°N, 180°W–120°W), and South Pacific (70°S–35°S, 160°E–70°W). [e]ATom vertical profiles are separated into North Atlantic (35°N–60°N, 60°W–0°E) and Central Atlantic (35°S–35°N, 40°W–0°E). [f]INTEX-B vertical profiles are calculated separately for the two aircraft: DC-8 (19°N–60°N, 175°E–120°W) and C-130 (35°N–55°N, 140°W–105°W). [g]PEM-Tropics A vertical profiles are separated into Central Pacific (35°S–35°N, 150°E–100°W), and South Pacific (70°S–35°S, 165°E–100°W).

observations overplotted (gridded to 4° × 5° resolution). The three figures use the same color scale to facilitate comparison between species. The $MeNO_3$ distributions are also shown over a larger range of values in Figure S2 to highlight observed (gridded) values of up to 80 ppbv that are not apparent in Figure 2 due to the saturated color scale. The same observation-model comparisons are also presented as average vertical profiles for each campaign in the supplement (Figures S3–S5). We compare all observations to a 2013 simulation but explore the sensitivity to changing emissions in section 6.

Both observations and model highlight differences in the global distributions of the three species that are consistent with their sources and lifetimes. Over much of the globe, $MeNO_3$ dominates the alkyl nitrate budget due to the large ocean source. The model generally captures the large-scale variability of $MeNO_3$, including the enhancements in the tropics and the southern high latitudes. The spatial structure is particularly well captured in the tropical marine boundary layer, where tying the ocean $MeNO_3$ concentrations to chlorophyll (as a proxy for nitrite availability) provides a better simulation of the $MeNO_3$ distribution than was achieved in a simulation using a latitude cutoff alone. In the free troposphere, the model underestimates the tropical

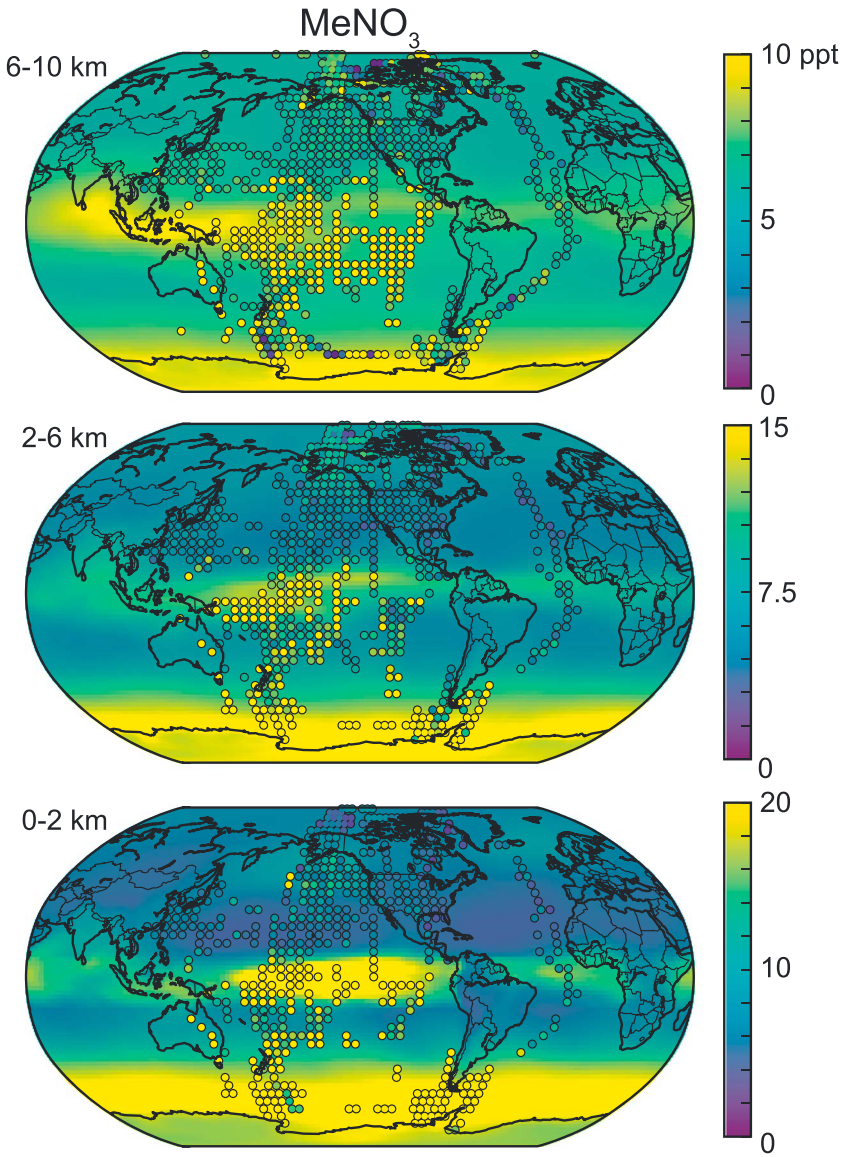

Figure 2. Annual mean distribution of methyl nitrate ($MeNO_3$) at different altitude ranges: 0–2 km (bottom), 2–6 km (middle), and 6–10 km (top). Solid background colors show model results from 2013 with aircraft observations from all years overplotted as filled circles. Observations have been averaged over all flight days and over a horizontal resolution of 4° × 5° for visibility. Note the difference in color scale between different altitude ranges.

observations by 30–50%, possibly due to insufficient convection. Evaluation against individual campaigns (Figure S3), however, suggests some discrepancy between the observations in this region. The model agrees well with the recent ATom campaigns (2016, 2017; mean bias = −1.0 ppt) but is biased low relative to the earlier HIPPO (2009–2011; mean bias = −5.8 ppt) and PEM-Tropics campaigns (1996, 1999; mean bias = −7.6 ppt), which measured nearly twice as much $MeNO_3$ in the free troposphere. As shown in section 6, trends in VOC and NO_x emissions are unlikely to be responsible for this difference. The discrepancy between the data sets remains unexplained, although interannual variability in convective activity and associated transport may play a role.

In the continental boundary layer and near-shore outflow regions, $PrNO_3$ is the dominant form of $RONO_2$. In these regions, elevated emissions of precursor VOCs combined with a higher yield for $PrNO_3$ formation than $MeNO_3$ or $EtNO_3$ drive enhanced $PrNO_3$ formation. However, the $PrNO_3$ lifetime is short, and enhancements generally drop off rapidly with altitude and with distance from source regions. The exception is in the Arctic

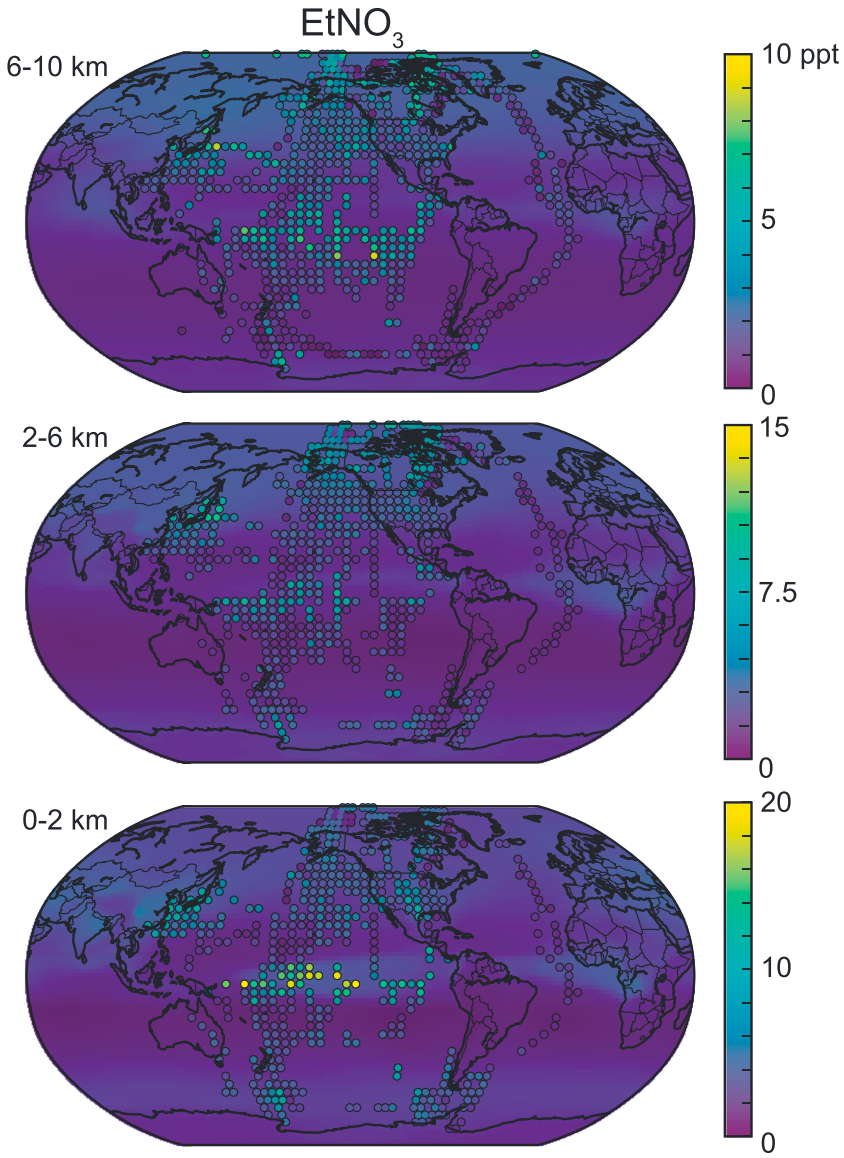

Figure 3. Same as Figure 2, but for ethyl nitrate ($EtNO_3$). The same color scales have been used to facilitate comparison between species.

free troposphere, where the observations show elevated $PrNO_3$. This may derive from Eurasian fossil fuel emissions, which are readily transported to the Arctic in spring (Fisher et al., 2010; Shindell et al., 2008) when both the ARCTAS and TOPSE campaigns took place (Table 2). The model underestimates the Arctic $PrNO_3$ enhancement (particularly in the western North American Arctic during ARCTAS) but overestimates Arctic propane, suggesting the simulated propane lifetime may be too long in Arctic spring. Previous work has suggested a small $PrNO_3$ source from the ocean (Atlas et al., 1993; Blake et al., 2003); we do not include that source here (section 2.1), leading to small biases in the marine boundary layer in the central and southern Pacific (Figure S5). Observed $PrNO_3$ in these regions is very low, and this bias has minimal impact on total $RONO_2$. Across the Pacific, low values in the free troposphere in both the model and the observations indicate $PrNO_3$ export is limited. Figure S6 shows that i-$PrNO_3$ is the dominant form of $PrNO_3$ everywhere, consistent with the higher yield of the isopropyl peroxy radical relative to the n-propyl peroxy radical (section 2.2).

$EtNO_3$ makes only a small contribution (<10 ppt) to total $RONO_2$ in all environments, as expected from its smaller ocean source than $MeNO_3$ and its lower yield of formation than $PrNO_3$. As for $MeNO_3$, the model generally reproduces the spatial variability of boundary layer $EtNO_3$, with moderately elevated concentrations

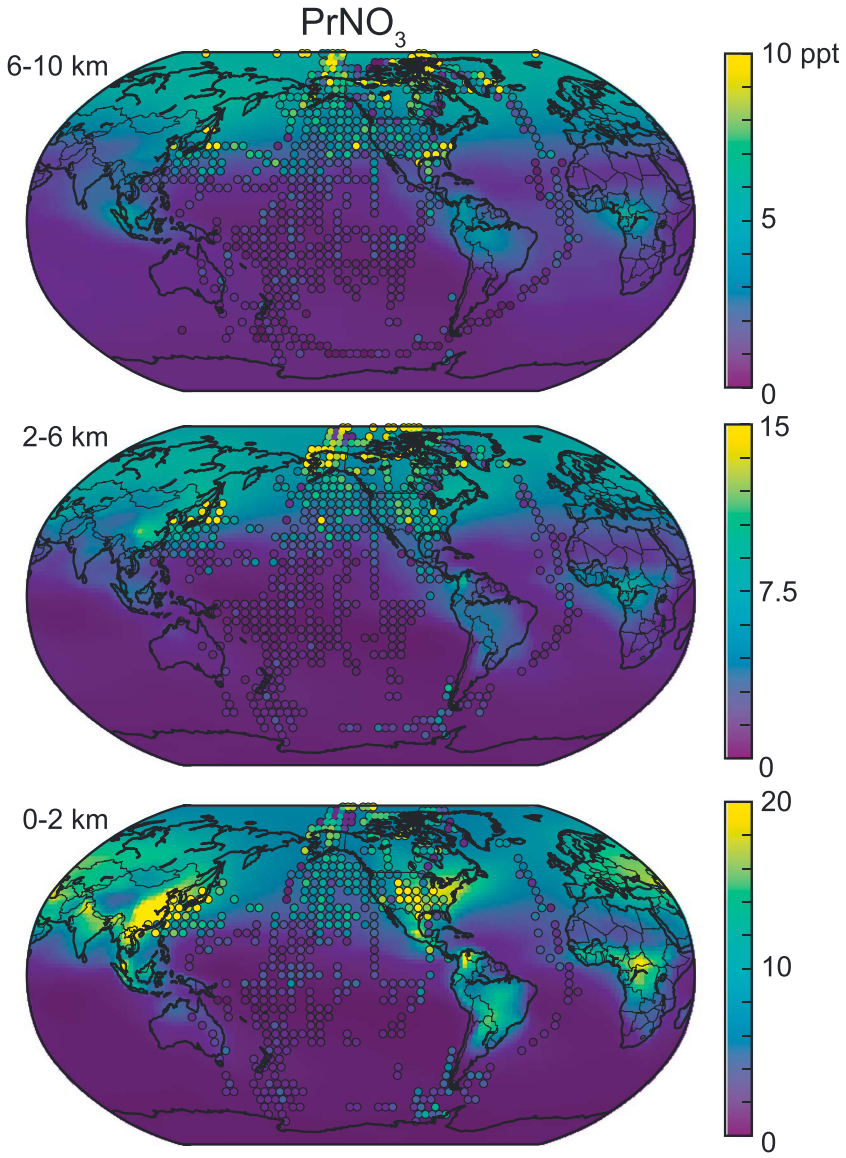

Figure 4. Same as Figure 2, but for propyl nitrate ($PrNO_3$). The same color scales have been used to facilitate comparison between species. See Figure S6 for separate maps of i-$PrNO_3$ and n-$PrNO_3$.

in the Southern Ocean, tropical Pacific, and parts of the North Pacific, but it is biased low throughout. In the tropical Pacific boundary layer, the low bias presumably reflects an underestimate in the prescribed ocean source (section 2.1). Elsewhere, the low bias is likely due to the treatment of the ethyl peroxy radical, which we assume here derives only from ethane oxidation but in reality has multiple chemical sources (see section 2.2). As such, our estimates of the $EtNO_3$ budget should be considered a lower limit. At only a few ppt, this bias has limited impact on the simulation of total $RONO_2$ and its impacts.

Figure 5 shows the seasonal distribution of total C_1-C_3 $RONO_2$ across a latitudinal transect through the Pacific Ocean (130–180°W). The model suggests there is little $RONO_2$ seasonality in the tropics, although large variability in the observations (driven by the campaign-level differences in $MeNO_3$ discussed above) makes this difficult to verify. In the northern extratropics (north of 30°N), both observations and model show higher concentrations in winter than summer driven by the increased $RONO_2$ lifetime against photolysis and oxidation. The model underestimates northern polar tropospheric $RONO_2$ in boreal spring (MAM), mainly reflecting the $PrNO_3$ underestimate described above.

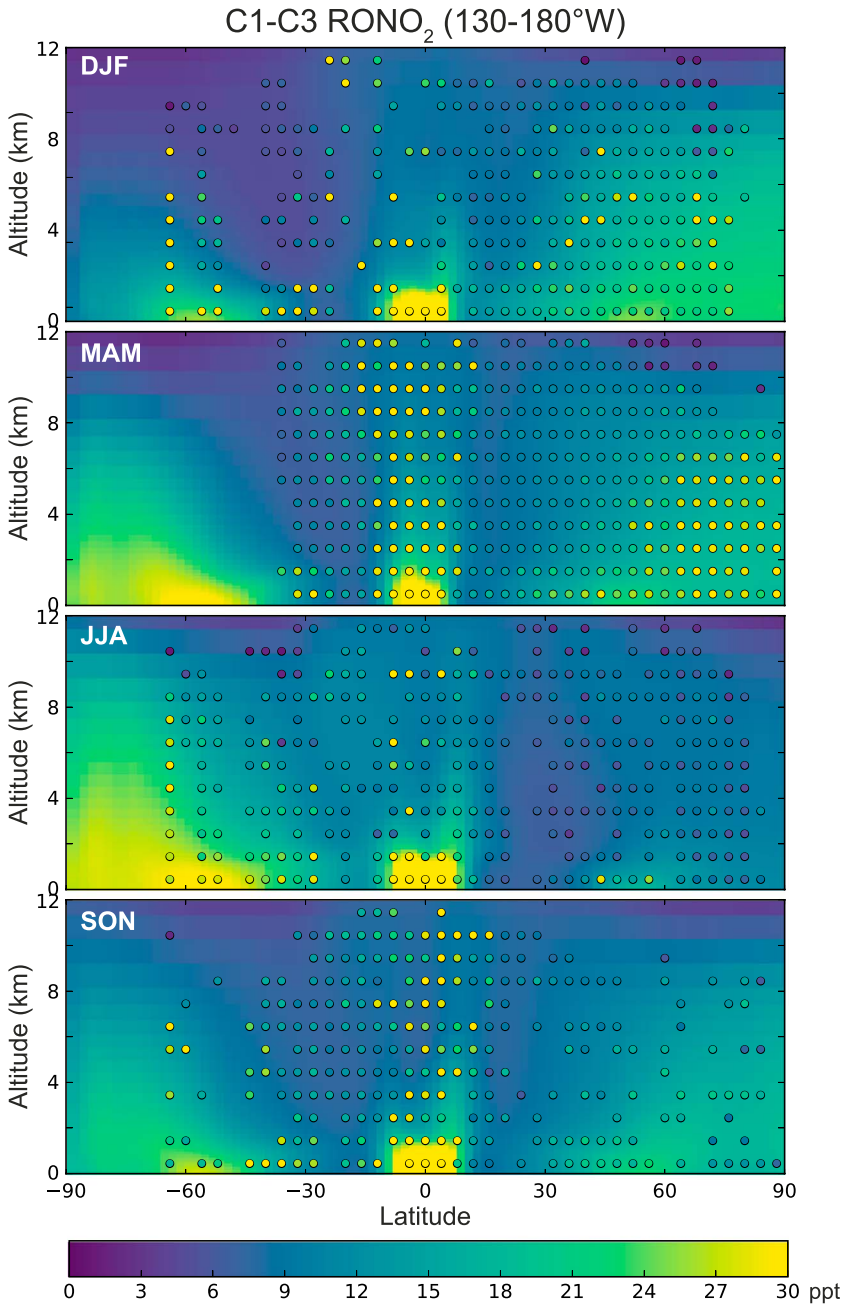

Figure 5. Zonal cross sections of seasonal mean distribution of total C_1-C_3 $RONO_2$ over the Pacific (130–180°W). Solid background colors show model results from 2013, with aircraft observations from all years overplotted as filled circles. Observations have been averaged over all flight days and over a horizontal resolution of 4° × 5° and vertical resolution of 1 km.

In the southern high latitudes, the ATom data (Figure S3) show $MeNO_3$ in the lower troposphere nearly doubles from ATom-1 in August 2016 (austral winter) to ATom-2 in February 2017 (austral summer). The summer enhancement may be linked to a seasonal maximum in $RONO_2$ production in the Southern Ocean, particularly if ocean biota play a role (Blake et al., 2003). GEOS-Chem does not capture the observed seasonality in this region, showing significant $MeNO_3$ underestimates during the summer ATom-2 and ORCAS campaigns (Figure S3). The summer biases are largest near the surface, where the model is too low by 24% (ORCAS) to 48% (ATom-2). The model assumes constant seawater $RONO_2$ concentrations in the Southern Ocean, with values based on measurements taken in November/December (Hughes et al., 2008). Although no other seawater measurements are available to constrain this seasonality, a limited atmospheric data set from the Antarctic

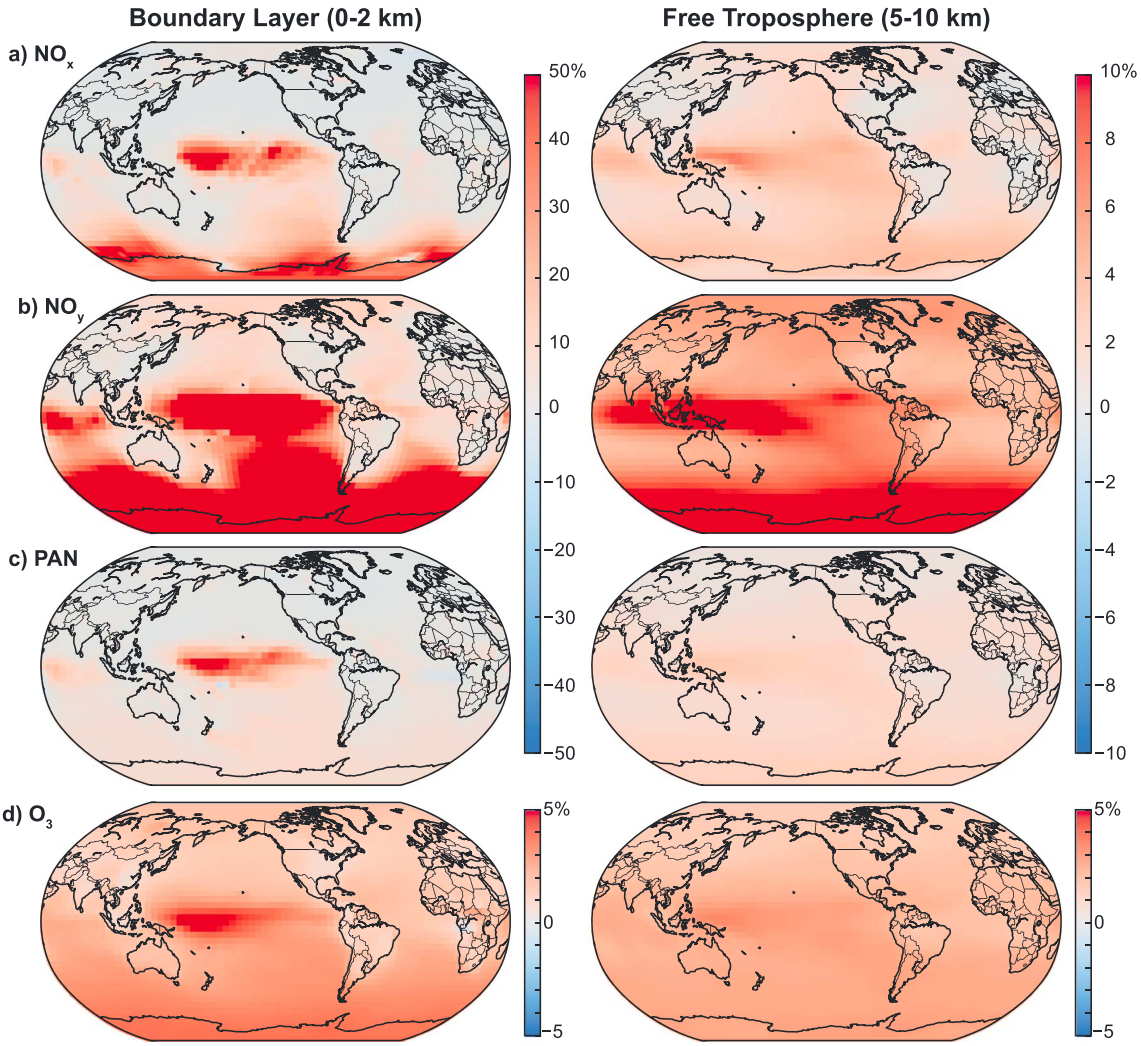

Figure 6. Relative change in annual mean (a) NO_x, (b) NO_y, (c) PAN, and (d) ozone caused by adding C_1-C_3 $RONO_2$ chemistry to GEOS-Chem. Changes are expressed as percent change from the standard simulation (no C_1-C_3 $RONO_2$) and shown separately for the boundary layer (0–2 km, left panels) and free troposphere (5–10 km, right panels). Absolute differences can be found in Figure S7.

continent suggests $MeNO_3$ increases throughout the summer (Jones et al., 1999). In late summer, seawater $RONO_2$ concentrations may therefore be higher than the early summer values used in the model, likely contributing to the atmospheric underestimate relative to the January–February ORCAS and ATom-2 data. Given the large contribution of $RONO_2$ to total reactive nitrogen in the southern high latitudes (see section 4), further observational constraints on seawater concentrations and fluxes in the Southern Ocean would provide significant value to atmospheric models.

4. Implications for Reactive Nitrogen and Ozone

We evaluate the impacts of C_1-C_3 $RONO_2$ by comparing the new simulation to a version of the model without these species but otherwise identical. Relative differences between the two simulations in both the boundary layer (0-2 km) and free troposphere (5–10 km) are shown in Figure 6 for NO_x, total reactive nitrogen ($NO_y \equiv NO_x + RONO_2 + PANs + HNO_3 +$ other nitrogen species), PAN, and ozone. Absolute differences can be found in Figure S7.

The impacts of including $RONO_2$ in the simulation are most pronounced in the marine boundary layer of the tropical Pacific and the Southern Ocean, coincident with the large $MeNO_3$ source. In the absence of ocean-derived $RONO_2$, these regions have virtually no reactive nitrogen sources, and the added $RONO_2$ act to more than double boundary layer NO_y from a baseline of 20–25 ppt. In the free troposphere (right panels of

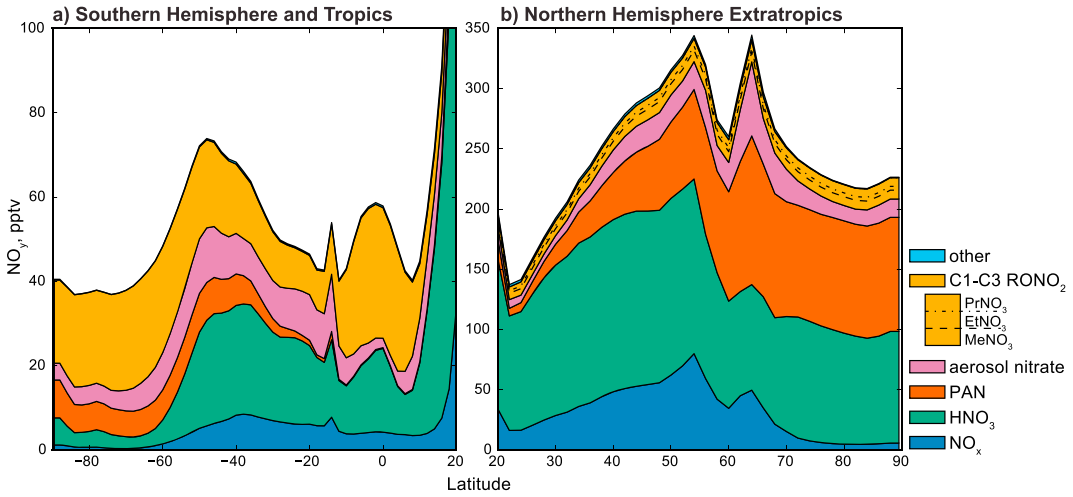

Figure 7. Simulated boundary layer (0–2 km) partitioning of NO_y as a function of latitude in the central Pacific Ocean (180–130°W).

Figures 6 and S7), NO_y increases nearly uniformly by 10–15 pptv, which equates to a nearly 20% enhancement over the tropical Pacific and Southern Ocean where NO_y is otherwise low. Increases in other NO_y components including NO_x and PAN appear large on a relative scale but are negligible (≤1 ppt) in absolute terms (Figure S7).

Despite the large increase in reactive nitrogen over the Pacific, the average increase in ozone is less than 1 ppb, equivalent to up to 6.2% in the tropical marine boundary layer and closer to 3% in the free troposphere. The small impact on ozone found here is more consistent with the recent findings from Williams et al. (2014) than with the earlier work by Neu et al. (2008), who found an increase of up to 20%. This difference is due in part to differences in the NO_x response to the introduction of $RONO_2$. While Neu et al. (2008) found a NO_x increase of up to 250%, we see a maximum NO_x increase of 100%, although the absolute change (≈1 ppt) and the spatial pattern of the change (maximum in the western Pacific) are similar between the two models. As in Williams et al. (2014), we find that marine boundary layer ozone is well buffered and has limited sensitivity to the presence of alkyl nitrates.

Figure 7 shows the simulated NO_y partitioning along a latitudinal transect through the Pacific marine boundary layer (0–2 km, 180–130°W). In the northern hemisphere, the $RONO_2$ contribution is small relative to NO_x, HNO_3, and PAN. In the southern hemisphere, however, $RONO_2$ (mainly $MeNO_3$) are a significant source of nitrogen to the marine boundary layer, responsible for 20–60% of total NO_y. Consistent with the difference maps, the $RONO_2$ contribution is particularly significant in the tropics (15°S – 10°N) and Southern Ocean (60–90°S), where it dominates the NO_y budget. We find that the addition of $RONO_2$ to the simulation has minimal impact on other NO_y components (Figure S8).

Without including short-chain $RONO_2$, the model significantly underestimates reactive nitrogen over the Southern Ocean. Figure 8 compares vertical profiles of Southern Ocean NO_y observed during ATom to the original and improved simulations. The prior simulation (blue) underestimated NO_y in the South Pacific marine boundary layer by a factor of three in August (ATom-1) and by a factor of 15 in February (ATom-2). The figure suggests that $RONO_2$ can explain much of this discrepancy. When these species are included in GEOS-Chem (red), the NO_y bias disappears in August and is improved in February (from 15× to 3× too low). About half of the remaining difference in February can be explained by the summer $RONO_2$ underestimate described in section 3 (Figure 8, middle).

Although the additional $RONO_2$ species greatly improve simulation of Southern Ocean NO_y, they do not explain a lingering model underestimate of NO_x in the region (Figure 8, bottom). Both the original and new simulations underestimate ATom NO_x observations by a factor of 5–10 in the lower troposphere, with even larger underestimates at the surface in February (ATom-2). There is negligible difference in NO_x between the two simulations, implying that $RONO_2$ degradation is not an important source of NO_x to the Southern Ocean in the model. It is possible that the modeled $MeNO_3$ lifetime is too long, leading to an underestimate of $RONO_2$ loss and associated NO_2 release, although the lifetime (26 days, Table 2) is within the range of previous

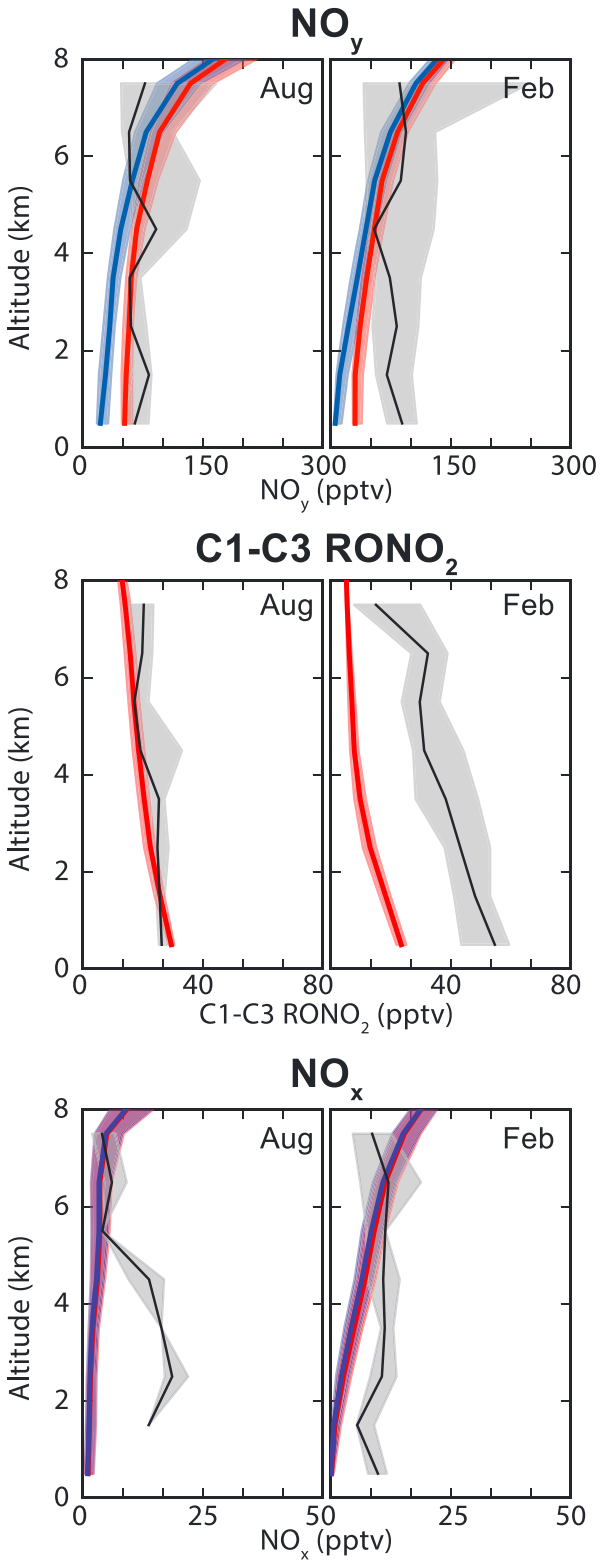

Figure 8. Observed (black) and simulated (red, blue) median vertical profiles of NO_y (top), C_1-C_3 $RONO_2$ (middle), and NO_x (bottom) over the Southern Ocean (50–70°S, 175°E–70°W) during ATom-1 (Aug 2016, left) and ATom-2 (Feb 2017, right). For NO_y and NO_x, the blue lines show the original simulation with no C_1-C_3 $RONO_2$ and the red lines show the new simulation. Solid lines represent the median value in 1-km altitude bins, and shading represents the interquartile range. The observed NO_x values shown here combine measured NO with NO_2 calculated from measured NO and O_3 assuming photostationary steady state.

estimates (Butkovskaya et al., 2012; Khan et al., 2015; Roberts & Fajer, 1989; Talukdar et al., 1997; Williams et al., 2014). If this is the case, our estimates of $RONO_2$ emission from the ocean are likely also too low, as faster atmospheric loss would require a larger source to match observed atmospheric mixing ratios.

An alternative explanation for the missing Southern Ocean NO_x in the model is direct NO emission from the ocean, a source not included in GEOS-Chem. While one fate for NO radicals in seawater is reaction with dissolved organic matter to form $RONO_2$, an alternative is diffusion to the marine surface layer and exchange with the atmosphere (driven by the low solubility of NO in water). NO efflux has been observed in the equatorial Pacific (Torres & Thompson, 1993; Zafiriou & McFarland, 1981) as well as inland seas (Anifowose & Sakugawa, 2017; Olasehinde et al., 2010), although it is typically much smaller than the deposition flux (Liu et al., 1983). Inclusion of a direct NO source from seawater could help reconcile observed and simulated atmospheric NO_x in the Southern Ocean. Measurements are needed to confirm whether this is a viable NO_x source in this region.

5. Contribution of Alkyl Nitrates to NO_x Export

The lifetimes of short-chain $RONO_2$ species are sufficiently long to allow their transport from sources to remote regions, and so they have the potential to serve as NO_x reservoirs. Chemical production of $RONO_2$ sequesters NO in high-emission source regions (reaction (4), while $RONO_2$ destruction via oxidation or photolysis releases NO_2 downwind. We use the new simulation to quantify the contribution of $RONO_2$ chemistry to NO_x export from source regions. For every model grid box, we calculate the net NO_x source/sink from $RONO_2$ chemistry ($\Delta NO_x|_{RONO_2}$) as the difference between NO consumed during $RONO_2$ formation ($L(NO_x)|_{RONO_2}$) and NO_2 released during $RONO_2$ destruction ($P(NO_x)|_{RONO_2}$):

$$\Delta NO_x|_{RONO_2} = P(NO_x)|_{RONO_2} - L(NO_x)|_{RONO_2} \quad (5)$$

We include here all $RONO_2$ species in the model mechanism (which also includes isoprene hydroxynitrates, monoterpene hydroxynitrates, and $\geq C_4$ alkyl nitrates from higher alkanes) to fully quantify the $RONO_2$ impact but expect the C_1-C_3 species to dominate export due to their longer lifetimes.

Figures 9a and 9b (top panels) shows the net NO_x source associated with $RONO_2$ chemistry. Orange pixels indicate net NO_x release (i.e., more NO_2 released than consumed in a given location) and purple pixels indicate net NO_x consumption. The figure shows that $RONO_2$ are net NO_x sinks in continental regions, where emissions of precursors drive $RONO_2$ formation and associated NO consumption. In the tropics and southern hemisphere, $RONO_2$ are net NO_x sources over the oceans, presumably due to the direct ocean $RONO_2$ source coupled with a lack of precursors to enable in situ $RONO_2$ formation.

In contrast, $RONO_2$ drive net NO_x loss over the northern midlatitude oceans in regions of continental outflow. This result implies that $RONO_2$ do not effectively export NO_x from high-emission source regions to downwind ocean regions. The model indicates that $RONO_2$ destruction does occur in the northern midlatitude continental outflow but is outweighed by in situ $RONO_2$ production (Figure S9). $RONO_2$ production requires available NO, implying the existence of a source of NO in the continental outflow from either primary emissions (e.g., shipping at the surface, aircraft and lightning in the free troposphere) or chemical recycling. In the lower troposphere, PAN decomposition can be a significant source of NO_x to the continental outflow, as discussed below.

We compare the net NO_x source from $RONO_2$ chemistry to the equivalent source from PAN in Figures 9c, 9d, and S10. PAN is stable at the cold temperatures of the mid–upper troposphere but unstable in the boundary layer. As a result, there is a strong vertical gradient in the net NO_x source from PAN, with NO_x release near the surface and NO_x consumption at higher altitude. The PAN-derived NO_x source is enhanced in the low-altitude continental outflow over the northern midlatitudes, contributing to the NO_x available for $RONO_2$ production.

Outside the northern midlatitude continental outflow, both $RONO_2$ and PAN are net sources of NO_x to the marine boundary layer. The source from PAN (Figure 9c) is generally larger than the source from $RONO_2$ (Figure 9a), except over the tropical Pacific. Here PAN mixing ratios are at a minimum due to limited transport from source regions. At the same time, $RONO_2$ mixing ratios are enhanced by the direct ocean source. As a result, $RONO_2$ chemistry dominates the chemical NO_x source over the tropical marine boundary layer. In the free troposphere, the NO_x source from $RONO_2$ (Figure 9b) partly compensates for the NO_x sink to PAN formation (Figure 9d).

The bottom row in Figure 9 compares NO_x from $RONO_2$ to primary NO_x emissions, shown as the ratio between the two sources. As $RONO_2$ are a net sink for NO_x over the continents, the comparisons are only shown over the

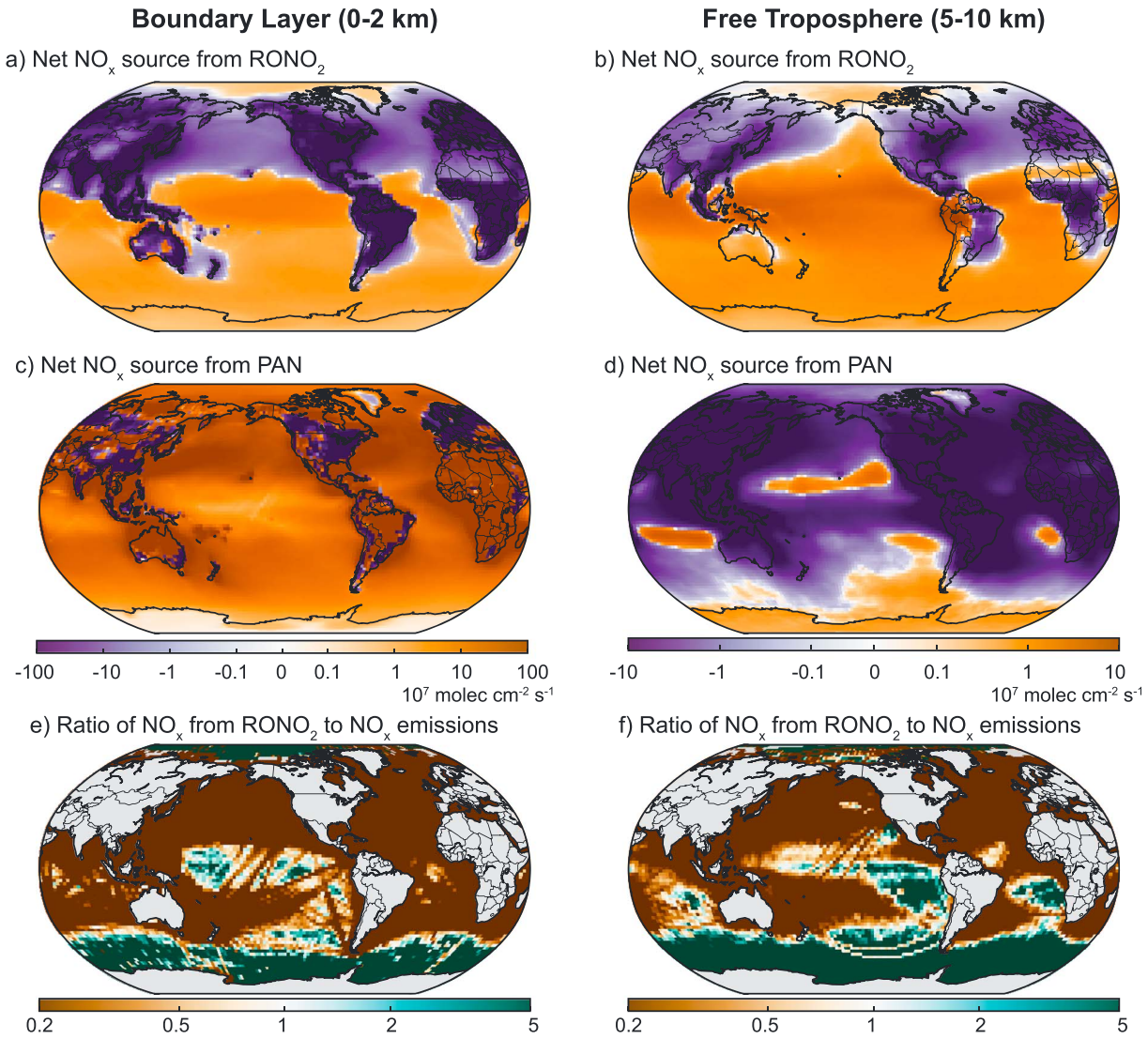

Figure 9. Impact of $RONO_2$ and PAN chemistry on NO_x export in the boundary layer (0–2 km, left) and free troposphere (5–10 km, right). The net NO_x source from $RONO_2$ (a and b) is calculated as the difference between NO_2 release during $RONO_2$ decomposition and NO consumption during $RONO_2$ formation, and summed over model levels within the given altitude range. Orange areas indicate net NO_x release and purple indicate net NO_x loss. The net NO_x source from PAN (c and d) is calculated the same way. Note that the boundary layer and free troposphere values cannot be directly compared as they represent different altitudinal extents. The bottom figures (e and f) show the ratio between the NO_x source from $RONO_2$ and NO_x emissions over the oceans. Areas with no net NO_x release from $RONO_2$ are shown in brown, and those with no NO_x emissions are shown in green.

ocean. In most regions, the NO_x source from $RONO_2$ is much smaller than the source from primary emissions (shipping, aircraft, and lightning). The two sources are roughly equivalent in parts of the tropics, where the ocean provides a direct $RONO_2$ source and primary emissions are low (outside major shipping and aircraft routes). Over the Southern Ocean where there are virtually no primary emissions, the NO_x source from $RONO_2$ degradation dominates relative to the source from primary emissions. Although the absolute amount of NO_x associated with the $RONO_2$ source is small, this result suggests a potentially significant perturbation to the chemistry of the Southern Ocean. Proper evaluation of the implications requires better understanding of the $RONO_2$ source in this region.

6. Sensitivity to Changing Emissions

In recent years, both NO_x and VOC emissions have changed dramatically. While global NO_x emissions have only grown slightly since 2000, there have been major changes in the distribution of source regions. Growing emissions from Asia, Africa, and Latin America have counteracted reductions in North America and Europe

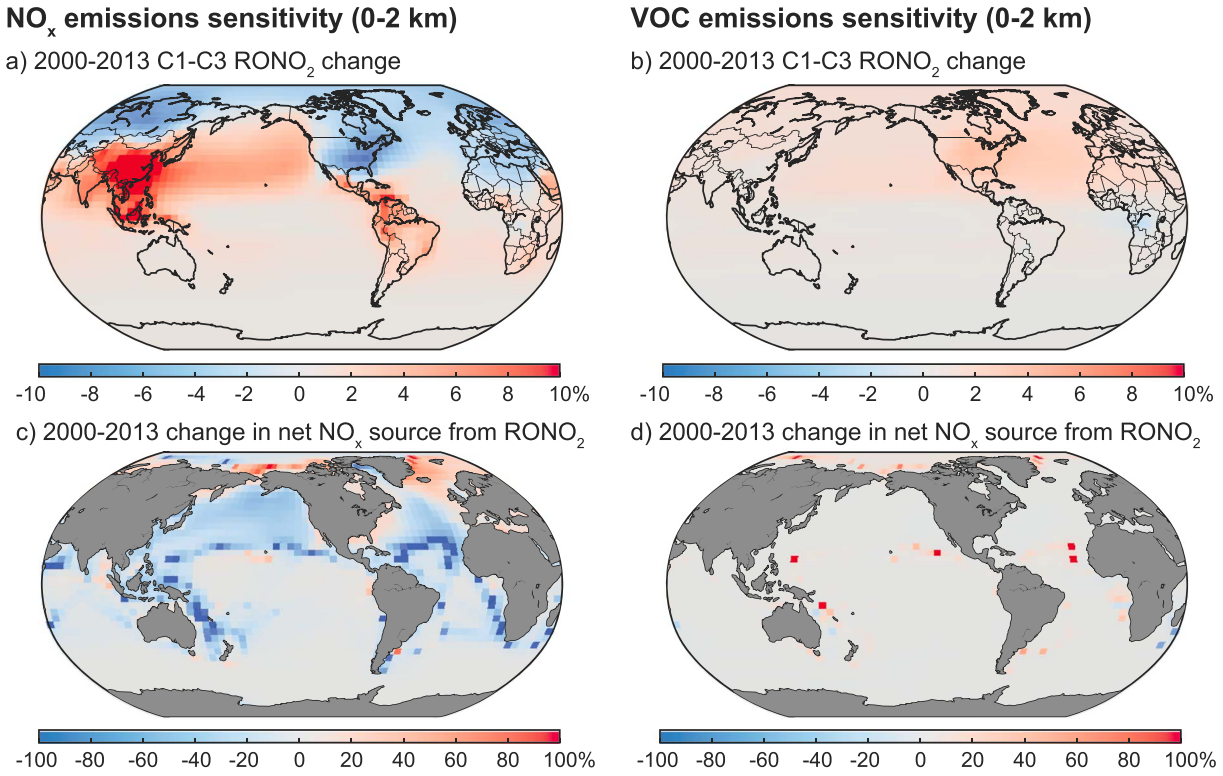

Figure 10. Sensitivity of boundary layer (0–2 km) C_1–C_3 $RONO_2$ (a and b) and related chemistry (c and d) to 2000–2013 changes in NO_x emissions (left) and VOC emissions (right). The net NO_x source from $RONO_2$ chemistry (c and d) is calculated as described in the text and in Figure 9; for clarity, only changes over the ocean are shown.

(Hoesly et al., 2018). Meanwhile, long-term declines in ethane and propane in the northern hemisphere (Aydin et al., 2011; Helmig et al., 2014; Simpson et al., 2012) reversed in 2009 with significant growth linked to U.S. oil and gas extraction (Franco et al., 2016; Helmig et al., 2016). Around the same time, methane growth resumed after a stable period in the early 2000s (Schaefer et al., 2016). These changes to precursor emissions have implications for $RONO_2$. Here we explore the sensitivity of the GEOS-Chem $RONO_2$ simulation to emission trends since 2000.

We performed three sensitivity simulations that are identical to the base simulation except using year 2000 emissions for (1) NO_x only, (2) VOCs (methane, ethane, and propane) only, and (3) both NO_x and VOCs. The combined impact of changing both NO_x and VOC emissions was nearly identical to the impact of changing NO_x emissions alone, and so we do not discuss this simulation further. As described in section 2.3, NO_x and VOC emissions in our base simulation are derived by combining multiple inventories, with global emissions overwritten where available by regional inventories. Each inventory was originally derived using different methodologies and different base years (and so our "2013" emissions actually represent an amalgam of different years). As a result, it is not straightforward to simulate the impact of emission trends by replacing the "2013" base emissions with emissions from a global inventory for a different year.

Instead, we evaluate the relative change from 2000 to 2013 by applying regional scaling factors to the base emissions. Scaling factors are detailed in Table S2. NO_x scaling factors were calculated using the Community Emission Data System (Hoesly et al., 2018), applied separately for the aggregated regions defined therein (China, other Asia, Europe, Former Soviet Union, North America, Latin America, Africa, and global shipping). Ethane and propane scaling factors for North America were derived from Helmig et al. (2016) and Helmig et al. (2014); elsewhere, we assume no meaningful trends in alkane emissions. Methane in our simulation is prescribed globally from surface in situ measurements (section 2.3), and so we use the observed 2000 values rather than applying a scaling factor.

Figure 10 shows that boundary layer $RONO_2$ and related chemistry are more sensitive to 2000–2013 changes in NO_x emissions (left panels) than changes in VOC emissions (right panels). Most of the change in total C_1–C_3

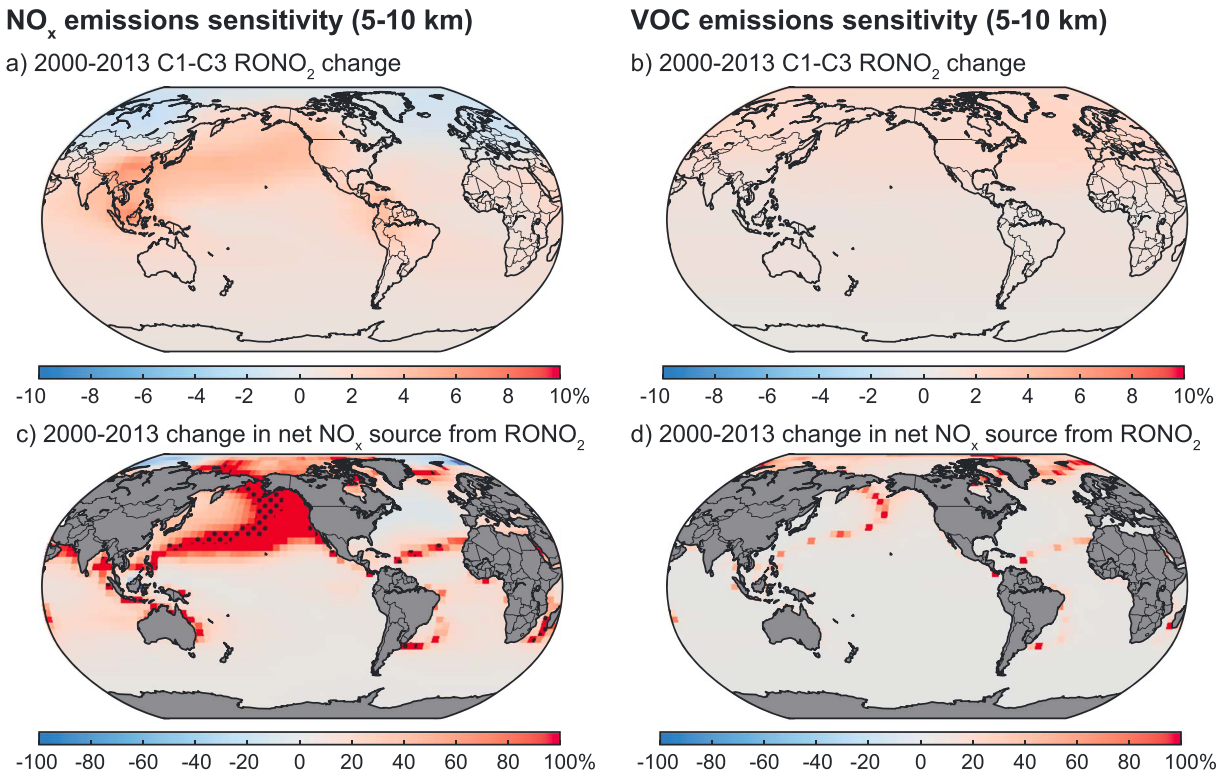

Figure 11. Same as Figure 10, but for the free troposphere (5–10 km). Stippling in (c) and (d) highlights regions where $RONO_2$ changes from a net NO_x sink with 2000 emissions to a net NO_x source with 2013 emissions.

$RONO_2$ (Figures 10a and 10b) is found over the continental source regions, where it mirrors the changes in precursors (Table S2). Impacts are generally negligible over the oceans. The exception is the North Pacific, where the growth in East Asian NO_x emissions has led to enhanced export of $RONO_2$. Changes in the free troposphere are similar but more diffuse (Figure 11).

We also evaluate the implications for NO_x export via $RONO_2$ chemistry using $\Delta NO_x|_{RONO_2}$ (section 5), shown in Figures 10c and 10d for the boundary layer and Figures 11c and 11d for the free troposphere. In the marine boundary layer, changing NO_x emissions have largely driven decreases in the NO_x source from $RONO_2$. This suggests that a substantial fraction of the increased boundary layer $RONO_2$ in the continental outflow (Figure 10a) is formed in situ over the oceans and that this $RONO_2$ production is in general NO_x-limited.

The situation is different in the free troposphere (Figures 11c and 11d). Here $\Delta NO_x|_{RONO_2}$ increases across the North Pacific, including in the eastern North Pacific where $RONO_2$ are already a net NO_x source (orange regions in Figure 9). The figure also shows that for some regions in the central North Pacific, $RONO_2$ transition from being a net NO_x sink in 2000 to a net NO_x source by 2013. In other words, these results suggest $RONO_2$ have become increasingly important reservoirs for exporting NO_x from Asia to the North Pacific free troposphere. We expect this additional NO_x source to negatively impact air quality in the western United States by promoting free tropospheric ozone formation followed by subsidence into the boundary layer (Liang et al., 2004; Lin et al., 2012; L. Zhang et al., 2009).

7. Conclusions

We have used a 20-year record of airborne observations combined with the GEOS-Chem chemical transport model to better understand the global sources, distribution, and impacts of three short-chain alkyl nitrates ($RONO_2$): methyl nitrate ($MeNO_3$), ethyl nitrate ($EtNO_3$), and propyl nitrate ($PrNO_3$). We modified GEOS-Chem to include the atmospheric chemical production and loss of these species, as well as their exchange with the ocean, and evaluated the simulation using the airborne observations. We then used the model to quantify the global budget and distribution of $MeNO_3$, $EtNO_3$, and $PrNO_3$, their impacts on NO_x, reactive nitrogen, and ozone (including through long-range export), and their sensitivity to recent changes in precursor emissions.

Our updated model provides for the first time a mechanistic treatment of bidirectional $RONO_2$ air-sea exchange. The new exchange parameterization ties in situ seawater $RONO_2$ to the distribution of nitrite, a limiting factor for $RONO_2$ production (Dahl & Saltzman, 2008; Dahl et al., 2012), with seawater concentrations based on the few existing waterside measurements (Dahl et al., 2007; Hughes et al., 2008). The bidirectional exchange parameterization improves on prior work by allowing the ocean to serve as both a source and a sink for $RONO_2$, with both spatial and temporal variability driven by changes in temperature, wind speed, and available nitrite. With the inclusion of bidirectional $RONO_2$ ocean exchange combined with updates to the atmospheric chemistry and the precursor emissions, the GEOS-Chem $RONO_2$ simulation is generally consistent with the ensemble of airborne observations.

Both observations and model show that $MeNO_3$ accounts for the majority of global C_1-C_3 $RONO_2$ (64%). $MeNO_3$ is the dominant form of $RONO_2$ everywhere except the continental boundary layer, where $PrNO_3$ (dominated by i-$PrNO_3$) is more abundant due to a higher yield of formation combined with elevated precursors. However, the short $PrNO_3$ lifetime limits its contribution on the global scale (22%). $EtNO_3$ makes the smallest contribution globally (14%), although this should be treated as a lower limit as the model does not include $EtNO_3$ formation from sources other than ethane. Nonetheless, both model and observations show $EtNO_3$ concentrations that are substantially lower than $MeNO_3$ in marine environments and lower than $PrNO_3$ in continental environments. The large ensemble of aircraft campaigns conducted at different times of year over the Pacific provides a unique opportunity to evaluate $RONO_2$ seasonal variability. We find that the model captures the observed seasonality over the North Pacific, driven by the $RONO_2$ lifetime, and the lack of seasonality over the tropics. Over the South Pacific, GEOS-Chem underestimates the observed austral summer peak in $MeNO_3$ by roughly 50%. Better understanding of Southern Ocean seawater $RONO_2$ sources and ensuing fluxes is needed to improve $RONO_2$ simulations in this region.

We find in the model that $MeNO_3$ makes a large contribution to reactive nitrogen (NO_y) in the southern hemisphere marine boundary layer, particularly across the Southern Ocean where other NO_y sources are minimal. Here $MeNO_3$ accounts for up to half of total simulated NO_y and corrects a large model NO_y underestimate relative to the ATom-1 aircraft observations (although the model remains low relative to the austral summer ATom-2 data). More modest impacts are seen for ozone, which increases by 6% in the tropical marine boundary layer but closer to 3% elsewhere. Impacts on marine NO_x are also small, with increases that are less than 1 pptv in absolute terms. Despite the introduction of a large $RONO_2$ source in the Southern Ocean, simulated NO_x in this region remains too low by a factor of 20. This large bias points to a missing NO_x source, possibly linked to direct NO emission from seawater, and requires further investigation.

The model indicates that $RONO_2$ do not play an important role in exporting NO_x from continental source regions to the remote marine environment. In fact, over the northern midlatitudes, the polluted continental outflow is sufficiently enriched in $RONO_2$ precursors that $RONO_2$ production (NO_x consuming) outweighs $RONO_2$ degradation (NO_x releasing). Elsewhere, ocean-derived $RONO_2$ largely serve as a small net NO_x source. This source is generally smaller than the source from PAN degradation or from direct emissions but does become important in parts of the tropical free troposphere outside major aircraft and shipping channels.

Over the past decade, emissions of $RONO_2$ precursors have changed across the globe in response to both air quality policy and growing energy needs. We find using model sensitivity studies that growth in precursor VOCs since 2000 has had little impact on C_1-C_3 $RONO_2$. In contrast, increasing East Asian NO_x emissions have driven modest growth in North Pacific $RONO_2$ and an associated increase in net NO_x release in the remote free troposphere. While further increases in East Asian NO_x emissions are unlikely, business-as-usual scenarios predict substantial NO_x emissions growth in southern Africa, South America, and Southeast Asia (Turnock et al., 2018). Our results imply that such growth may lead to enhanced $RONO_2$ and associated NO_x release over downwind ocean regions in the southern hemisphere and tropics—regions that are already among the most sensitive to $RONO_2$ cycling.

Acronyms

ATom Atmospheric Tomography
DC3 Deep Convective Clouds and Chemistry
GEOS Goddard Earth Observing System
NEI National Emissions Inventory

Acknowledgments
We gratefully acknowledge the many contributors to all aspects of the 19 aircraft campaigns included here. We also thank Elisabeth Dahl for helpful discussions about the ocean source of alkyl nitrates. This work was funded in part by ARC Discovery Project DP160101598 and was undertaken with the assistance of resources provided at the NCI National Facility systems at the Australian National University through the National Computational Merit Allocation Scheme supported by the Australian Government. E. L. A. acknowledges contributions from F. Flocke, S. Schauffler, R. Lueb, R. Hendershot, V. Stroud, V. Donets, X. Zhu, M. Navarro, and L. Pope, and financial support in several grants from NASA and and the NSF Atmospheric Chemistry Program. Funding for Z. A. T. -S. was provided by Consejo Nacional de Ciencia y Tecnología (CONACYT) under fellowship 216028 and NOAA under award NA14OAR4310148. Funding for ATom NO_y measurements was provided by the NASA Earth Venture Suborbital-2 program NNH15AB12I. Aircraft data used in this work are available from the Toolsets for Airborne Data Web Application (https://tad.larc.nasa.gov/login.php) for ARCTAS, INTEX, and TEXAQS; the NASA Airborne Science Data for Atmospheric Composition archive (https://www-air.larc.nasa.gov/index.html) for DC3, FRAPPE, SEAC4RS, and TRACE-P; the Global Tropospheric Experiment archive (https://www-gte.larc.nasa.gov/gte_miss.htm) for PEM-Tropics; the NCAR/UCAR Earth Observing Laboratory archive (https://www.eol.ucar.edu/all-field-projects-and-deployments) for HIPPO, ORCAS, and TOPSE; the NOAA Earth Systems Research Laboratory Chemical Sciences Division for ITCT (https://esrl.noaa.gov/csd/projects/itct/2k2/); and the NASA Earth Science Project Office Data Archive (https://espoarchive.nasa.gov/archive/browse) for ATom. Note that calibration procedures were changed in 2008, so data from earlier aircraft campaigns (PEM-Tropics, TOPSE, TRACE-P, ITCT, INTEX, and TEXAQS) would need to be scaled as described in section 3 to reproduce the values used in this work. The standard GEOS-Chem code is freely accessible to the public by following the guidelines at http://geos-chem.org/. Updates described here will be included in the standard code once this paper has been accepted. In the interim, the modified version 9-02 code used here is available from https://github.com/jennyfisher/Code.v9-02.C1-C3_RONO2 with associated run directory files available from https://github.com/jennyfisher/C1-C3_RONO2_chemistry.

ORCAS O2/N2 Ratio and CO2 Airborne Southern Ocean Study
PAN peroxy acetyl nitrate
PANs Peroxyacyl Nitrates
VOC volatile organic compound

References

Akagi, S. K., Yokelson, R. J., Wiedinmyer, C., Alvarado, M. J., Reid, J. S., Karl, T., et al. (2011). Emission factors for open and domestic biomass burning for use in atmospheric models. *Atmospheric Chemistry and Physics*, *11*(9), 4039–4072.

Anifowose, A. J., & Sakugawa, H. (2017). Determination of daytime flux of nitric oxide radical (NO●) at an inland sea-atmospheric boundary in Japan. *Journal of Aquatic Pollution and Toxicology*, *1*(2), 1–6.

Atkinson, R., Aschmann, S. M., Carter, W. P. L., Winer, A. M., & Pitts, J. N. (1982). Alkyl nitrate formation from the nitrogen oxide (NO_x)-air photooxidations of C2-C8 n-alkanes. *The Journal of Physical Chemistry*, *86*(23), 4563–4569.

Atlas, E., Pollock, W., Greenberg, J., Heidt, L., & Thompson, A. M. (1993). Alkyl nitrates, nonmethane hydrocarbons, and halocarbon gases over the equatorial Pacific Ocean during SAGA 3. *Journal of Geophysical Research*, *98*(D9), 16,933–16,947.

Atlas, E. L., & UCAR/NCAR-Earth Observing Laboratory (2009). Advanced Whole Air Sampler (AWAS) for HIAPER.

Aydin, M., Verhulst, K. R., Saltzman, E. S., Battle, M. O., Montzka, S. A., Blake, D. R., et al. (2011). Recent decreases in fossil-fuel emissions of ethane and methane derived from firn air. *Nature*, *476*(7359), 198–201.

Bian, H., & Prather, M. J. (2002). Fast-J2: Accurate simulation of stratospheric photolysis in global chemical models. *Journal of Atmospheric Chemistry*, *41*(3), 281–296.

Blake, N. J., Blake, D. R., Swanson, A. L., Atlas, E., Flocke, F., & Rowland, F. S. (2003). Latitudinal, vertical, and seasonal variations of C1-C4 alkyl nitrates in the troposphere over the Pacific Ocean during PEM-Tropics A and B: Oceanic and continental sources. *Journal of Geophysical Research*, *108*(D2), 8242. https://doi.org/10.1029/2001JD001444

Blake, N. J., Blake, D. R., Wingenter, O. W., Sive, B. C., Kang, C. H., Thornton, D. C., et al. (1999). Aircraft measurements of the latitudinal, vertical, and seasonal variations of NMHCs, methyl nitrate, methyl halides, and DMS during the First Aerosol Characterization Experiment (ACE 1). *Journal of Geophysical Research*, *104*(D17), 21,803–21,817.

Butkovskaya, N., Kukui, A., & Le Bras, G. (2009). Pressure and temperature dependence of ethyl nitrate formation in the C2H5O2 + NO reaction. *The Journal of Physical Chemistry A*, *114*(2), 956–964.

Butkovskaya, N., Kukui, A., & Le Bras, G. (2012). Pressure and temperature dependence of methyl nitrate formation in the CH3O2 + NO reaction. *The Journal of Physical Chemistry A*, *116*(24), 5972–5980.

Carter, W. P. L., & Atkinson, R. (1989). Alkyl nitrate formation from the atmospheric photoxidation of alkanes: A revised estimation method. *Journal of Atmospheric Chemistry*, *8*(2), 165–173.

Chuck, A. L. (2002). Direct evidence for a marine source of C1 and C2 alkyl nitrates. *Science*, *297*(5584), 1151–1154.

Clemitshaw, K. C., Williams, J., Rattigan, O. V., Shallcross, D. E., Law, K. S., & Anthony Cox, R. (1997). Gas-phase ultraviolet absorption cross-sections and atmospheric lifetimes of several C2-C5 alkyl nitrates. *Journal of Photochemistry and Photobiology A: Chemistry*, *102*(2-3), 117–126.

Colman, J. J., Swanson, A. L., Meinardi, S., Sive, B. C., Blake, D. R., & Rowland, F. S. (2001). Description of the analysis of a wide range of volatile organic compounds in whole air samples collected during PEM-Tropics A and B. *Analytical Chemistry*, *73*(15), 3723–3731.

Dahl, E. E., Heiss, E. M., & Murawski, K. (2012). The effects of dissolved organic matter on alkyl nitrate production during GOMECC and laboratory studies. *Marine Chemistry*, *142-144*, 11–17.

Dahl, E. E., & Saltzman, E. S. (2008). Alkyl nitrate photochemical production rates in North Pacific seawater. *Marine Chemistry*, *112*(3-4), 137–141.

Dahl, E. E., Saltzman, E. S., & de Bruyn, W. J. (2003). The aqueous phase yield of alkyl nitrates from ROO + NO: Implications for photochemical production in seawater. *Geophysical Research Letters*, *30*(6), 919. https://doi.org/10.1029/2003GL018686

Dahl, E. E., Yvon Lewis, S. A., & Saltzman, E. S. (2005). Saturation anomalies of alkyl nitrates in the tropical Pacific Ocean. *Geophysical Research Letters*, *32*, L20817. https://doi.org/10.1029/2005GL023896

Dahl, E. E., Yvon Lewis, S. A., & Saltzman, E. S. (2007). Alkyl nitrate (C1-C3) depth profiles in the tropical pacific ocean. *Journal of Geophysical Research*, *112*, C01012. https://doi.org/10.1029/2006JC003471

Dalsøren, S. B., Myhre, G., Hodnebrog, Ø., Myhre, C. L., Stohl, A., Pisso, I., et al. (2018). Discrepancy between simulated and observed ethane and propane levels explained by underestimated fossil emissions. *Nature Geoscience*, *11*(3), 178–184.

Darmenov, A. S., & Da Silva, A. (2013). The quick fire emissions dataset (QFED)—Documentation of versions 2.1, 2.2 and 2.4 (Tech. Rep. NASA/TM-2013-104606/). Maryland, USA: Greenbelt.

Dibble, T. S. (2008). Failures and limitations of quantum chemistry for two key problems in the atmospheric chemistry of peroxy radicals. *Atmospheric Environment*, *42*(23), 5837–5848.

Farmer, D. K., Perring, A. E., Wooldridge, P. J., Blake, D. R., Baker, A., Meinardi, S., et al. (2011). Impact of organic nitrates on urban ozone production. *Atmospheric Chemistry and Physics*, *11*(9), 4085–4094.

Fischer, E. V., Jacob, D. J., Yantosca, R. M., Sulprizio, M. P., Millet, D. B., Mao, J., et al. (2014). Atmospheric peroxyacetyl nitrate (PAN): A global budget and source attribution. *Atmospheric Chemistry and Physics*, *14*(5), 2679–2698.

Fischer, R., Weller, R., Jacobi, H.-W., & Ballschmiter, K. (2002). Levels and pattern of volatile organic nitrates and halocarbons in the air at Neumayer station (70S), Antarctic. *Chemosphere*, *48*(9), 981–992.

Fisher, J. A., Jacob, D. J., Purdy, M. T., Kopacz, M., Le Sager, P., Carouge, C., et al. (2010). Source attribution and interannual variability of Arctic pollution in spring constrained by aircraft (ARCTAS, ARCPAC) and satellite (AIRS) observations of carbon monoxide. *Atmospheric Chemistry and Physics*, *10*(3), 977–996.

Fisher, J. A., Jacob, D. J., Travis, K. R., Kim, P. S., Marais, E. A., Chan Miller, C., et al. (2016). Organic nitrate chemistry and its implications for nitrogen budgets in an isoprene- and monoterpene-rich atmosphere: Constraints from aircraft ($SEAC_4RS$) and ground-based (SOAS) observations in the Southeast US. *Atmospheric Chemistry and Physics*, *16*, 5969–5991.

Flocke, F., Atlas, E., Madronich, S., Schauffler, S. M., Aikin, K., Margitan, J. J., & Bui, T. P. (1998). Observations of methyl nitrate in the lower stratosphere during STRAT: Implications for its gas phase production mechanisms. *Geophysical Research Letters*, *25*(11), 1891–1894.

Franco, B., Mahieu, E., Emmons, L. K., Tzompa-Sosa, Z. A., Fischer, E. V., Sudo, K., et al. (2016). Evaluating ethane and methane emissions associated with the development of oil and natural gas extraction in North America. *Environmental Research Letters*, *11*(4), 044010.

Geddes, J. A., & Martin, R. V. (2017). Global deposition of total reactive nitrogen oxides from 1996 to 2014 constrained with satellite observations of NO2 columns. *Atmospheric Chemistry and Physics*, *17*(16), 10,071–10,091.

Helmig, D., Petrenko, V., Martinerie, P., Witrant, E., Röckmann, T., Zuiderweg, A., et al. (2014). Reconstruction of Northern Hemisphere 1950–2010 atmospheric non-methane hydrocarbons. *Atmospheric Chemistry and Physics*, *14*(3), 1463–1483.

Helmig, D., Rossabi, S., Hueber, J., Tans, P., Montzka, S. A., Masarie, K., et al. (2016). Reversal of global atmospheric ethane and propane trends largely due to US oil and natural gas production. *Nature Geoscience*, *9*(7), 490–495.

Higgins, C. M., Evans, L. A., Lloyd-Jones, G. C., Shallcross, D. E., Tew, D. P., & Orr-Ewing, A. J. (2014). Quantum yields for photochemical production of NO_2 from organic nitrates at tropospherically relevant wavelengths. *The Journal of Physical Chemistry A*, *118*(15), 2756–2764.

Hoesly, R. M., Smith, S. J., Feng, L., Klimont, Z., Janssens-Maenhout, G., Pitkanen, T., et al. (2018). Historical (1750-2014) anthropogenic emissions of reactive gases and aerosols from the Community Emissions Data System (CEDS). *Geoscientific Model Development*, *11*, 369–408. https://doi.org/10.5194/gmd-11-369-2018

Horowitz, L. W., Liang, J., Gardner, G. M., & Jacob, D. J. (1998). Export of reactive nitrogen from North America during summertime: Sensitivity to hydrocarbon chemistry. *Journal of Geophysical Research*, *103*(D11), 13,451–13,476.

Hu, L., Jacob, D. J., Liu, X., Zhang, Y., Zhang, L., Kim, P. S., et al. (2017). Global budget of tropospheric ozone: Evaluating recent model advances with satellite (OMI), aircraft (IAGOS), and ozonesonde observations. *Atmospheric Environment*, *167*, 323–334.

Hudman, R. C., Jacob, D. J., Cooper, O. R., Evans, M. J., Heald, C. L., Park, R. J., et al. (2004). Ozone production in transpacific Asian pollution plumes and implications for ozone air quality in California. *Journal of Geophysical Research*, *109*, 39. https://doi.org/10.1029/2004JD004974

Hudman, R. C., Moore, N. E., Mebust, A. K., Martin, R. V., Russell, A. R., Valin, L. C., & Cohen, R. C. (2012). Steps towards a mechanistic model of global soil nitric oxide emissions: Implementation and space based-constraints. *Atmospheric Chemistry and Physics*, *12*(16), 7779–7795.

Hughes, C., Chuck, A. L., Turner, S. M., & Liss, P. S. (2008). Methyl and ethyl nitrate saturation anomalies in the Southern Ocean (36-65S, 30-70W). *Environmental Chemistry*, *5*(1), 11.

Johnson, M. T. (2010). A numerical scheme to calculate temperature and salinity dependent air-water transfer velocities for any gas. *Ocean Science*, *6*(4), 913–932.

Jones, A. E., Weller, R., Minikin, A., Wolff, E. W., Sturges, W. T., McIntyre, H. P., et al. (1999). Oxidized nitrogen chemistry and speciation in the Antarctic troposphere. *Journal of Geophysical Research*, *104*(D17), 21,355–21,366.

Kang, M., Kanno, C. M., Reid, M. C., Zhang, X., Mauzerall, D. L., Celia, M. A., et al. (2014). Direct measurements of methane emissions from abandoned oil and gas wells in Pennsylvania. *Proceedings of the National Academy of Sciences*, *111*(51), 18,173–18,177.

Katzenstein, A. S., Doezema, L. A., Simpson, I. J., Blake, D. R., & Rowland, F. S. (2003). Extensive regional atmospheric hydrocarbon pollution in the southwestern United States. *Proceedings of the National Academy of Sciences*, *100*(21), 11,975–11,979.

Khan, M. A. H., Cooke, M. C., Utembe, S. R., Morris, W. C., Archibald, A. T., Derwent, R. G., et al. (2015). Global modeling of the C1-C3 alkyl nitrates using STOCHEM-CRI. *Atmospheric Environment*, *123*(Part A), 256–267.

Kim, P. S., Jacob, D. J., Fisher, J. A., Travis, K., Yu, K., Zhu, L., et al. (2015). Sources, seasonality, and trends of southeast US aerosol: An integrated analysis of surface, aircraft, and satellite observations with the GEOS-chem chemical transport model. *Atmospheric Chemistry and Physics*, *15*(18), 10,411–10,433.

Kim, M. J., Michaud, J. M., Williams, R., Sherwood, B. P., Pomeroy, R., Azam, F., et al. (2015). Bacteria-driven production of alkyl nitrates in seawater. *Geophysical Research Letters*, *42*, 597–604. https://doi.org/10.1002/2014GL062865

Kuhns, H., Knipping, E. M., & Vukovich, J. M. (2005). Development of a United States-Mexico emissions inventory for the Big Bend Regional Aerosol and Visibility Observational (BRAVO) study. *Journal of the Air & Waste Management Association*, *55*(5), 677–692.

Lee, L., Wooldridge, P. J., Gilman, J. B., Warneke, C., de Gouw, J., & Cohen, R. C. (2014). Low temperatures enhance organic nitrate formation: Evidence from observations in the 2012 Uintah Basin winter ozone study. *Atmospheric Chemistry and Physics*, *14*(22), 12,441–12,454.

Liang, Q., Jaeglé, L., Jaffe, D. A., Weiss-Penzias, P., Heckman, A., & Snow, J. A. (2004). Long-range transport of Asian pollution to the northeast Pacific: Seasonal variations and transport pathways of carbon monoxide. *Journal of Geophysical Research*, *109*, D23S07. https://doi.org/10.1029/2003JD004402

Lin, M., Fiore, A. M., Horowitz, L. W., Cooper, O. R., Naik, V., & Holloway, J. (2012). Transport of Asian ozone pollution into surface air over the western United States in spring. *Journal of Geophysical Research*, *117*, D00V07. https://doi.org/10.1029/2011JD016961

Liu, F., Beirle, S., Zhang, Q., Dörner, S., He, K., & Wagner, T. (2016). NO_x lifetimes and emissions of cities and power plants in polluted background estimated by satellite observations. *Atmospheric Chemistry and Physics*, *16*(8), 5283–5298.

Liu, H., Crawford, J. H., Pierce, R. B., Norris, P., Platnick, S. E., Chen, G., et al. (2006). Radiative effect of clouds on tropospheric chemistry in a global three-dimensional chemical transport model. *Journal of Geophysical Research*, *111*, 6871. https://doi.org/10.1029/2005JD006403

Liu, S. C., McFarland, M., Kley, D., Zafiriou, O., & Huebert, B. (1983). Tropospheric NO_x and O_3 budgets in the equatorial Pacific. *Journal of Geophysical Research(1984-2012)*, *88*(C2), 1360–1368.

Mao, J., Jacob, D. J., Evans, M. J., Olson, J. R., Ren, X., Brune, W. H., et al. (2010). Chemistry of hydrogen oxide radicals (HO_x) in the Arctic troposphere in spring. *Atmospheric Chemistry and Physics*, *10*(13), 5823–5838.

Marais, E. A., Jacob, D. J., Jimenez, J. L., Campuzano-Jost, P., Day, D. A., Hu, W., et al. (2016). Aqueous-phase mechanism for secondary organic aerosol formation from isoprene: Application to the southeast United States and co-benefit of SO2 emission controls. *Atmospheric Chemistry and Physics*, *16*(3), 1603–1618.

Moore, R. M., & Blough, N. V. (2002). A marine source of methyl nitrate. *Geophysical Research Letters*, *29*(15), 1737. https://doi.org/10.1029/2002GL014989

Murray, L. T. (2016). Lightning NO_x and impacts on air quality. *Current Pollution Reports*, *2*(2), 115–133.

Murray, L. T., Jacob, D. J., Logan, J. A., Hudman, R. C., & Koshak, W. J. (2012). Optimized regional and interannual variability of lightning in a global chemical transport model constrained by LIS/OTD satellite data. *Journal of Geophysical Research*, *117*, 3851. https://doi.org/10.1029/2012JD017934

Nault, B. A., Garland, C., Wooldridge, P. J., Brune, W. H., Campuzano-Jost, P., Crounse, J. D., et al. (2016). Observational constraints on the oxidation of NO_x in the upper troposphere. *The Journal of Physical Chemistry A*, *120*(9), 1468–1478.

Neu, J. L., Lawler, M. J., Prather, M. J., & Saltzman, E. S. (2008). Oceanic alkyl nitrates as a natural source of tropospheric ozone. *Geophysical Research Letters*, *35*, L13814. https://doi.org/10.1029/2008GL034189

Olasehinde, E. F., Takeda, K., & Sakugawa, H. (2010). Photochemical production and consumption mechanisms of nitric oxide in seawater. *Environmental Science & Technology*, *44*(22), 8403–8408.

Olivier, J. G. J., & Berdowski, J. J. M. (2001). Global Emissions Sources and Sinks. In J. J. M. Berdowski, R. Guicherit, & B. J. Heij (Eds.), *The Climate System* (pp. 33–78). The Netherlands: Lisse.

Olsen, A., Key, R. M., van Heuven, S., Lauvset, S. K., Velo, A., Lin, X., et al. (2016). The Global Ocean Data Analysis Project version 2 (GLODAPv2)—An internally consistent data product for the world ocean. *Earth System Science Data*, *8*(2), 297–323.

Paulot, F., Jacob, D. J., & Henze, D. K. (2013). Sources and processes contributing to nitrogen deposition: An adjoint model analysis applied to biodiversity hotspots worldwide. *Environmental Science & Technology*, *47*(7), 3226–3233.
Perring, A. E., Bertram, T. H., Farmer, D. K., Wooldridge, P. J., Dibb, J., Blake, N. J., et al. (2010). The production and persistence of $\Sigma RONO_2$ in the Mexico City plume. *Atmospheric Chemistry and Physics*, *10*(15), 7215–7229.
Perring, A. E., Pusede, S. E., & Cohen, R. C. (2013). An observational perspective on the atmospheric impacts of alkyl and multifunctional nitrates on ozone and secondary organic aerosol. *Chemical Reviews*, *113*(8), 5848–5870.
Ranschaert, D. L., Schneider, N. J., & Elrod, M. J. (2000). Kinetics of the $C_2H_5O_2 + NO_x$ reactions: Temperature dependence of the overall rate constant and the $C_2H_5ONO_2$ branching channel of $C_2H_5O_2 + NO$. *The Journal of Physical Chemistry A*, *104*(24), 5758–5765.
Roberts, J. M., & Fajer, R. W. (1989). UV absorption cross sections of organic nitrates of potential atmospheric importance and estimation of atmospheric lifetimes. *ACS Publications*, *23*, 945–951.
Roberts, J. M., Parrish, D. D., Norton, R. B., Bertman, S. B., Holloway, J. S., Trainer, M., et al. (1996). Episodic removal of NO_y species from the marine boundary layer over the North Atlantic. *Journal of Geophysical Research*, *101*(D22), 28,947–28,960.
Romer, P. S., Duffey, K. C., Wooldridge, P. J., Allen, H. M., Ayres, B. R., Brown, S. S., et al. (2016). The lifetime of nitrogen oxides in an isoprene-dominated forest. *Atmospheric Chemistry and Physics*, *16*(12), 7623–7637.
Russo, R. S., Zhou, Y., Haase, K. B., Wingenter, O. W., Frinak, E. K., Mao, H., et al. (2010). Temporal variability, sources, and sinks of C1–C5 alkyl nitrates in coastal New England. *Atmospheric Chemistry and Physics*, *10*, 1865–1883.
Sander, R. (2015). Compilation of Henry's law constants (version 4.0) for water as solvent. *Atmospheric Chemistry and Physics*, *15*(8), 4399–4981.
Schaefer, H., Fletcher, S. E. M., Veidt, C., Lassey, K. R., Brailsford, G. W., Bromley, T. M., et al. (2016). A 21st-century shift from fossil-fuel to biogenic methane emissions indicated by $^{13}CH_4$. *Science*, *352*(6281), 80–84.
Shindell, D. T., Chin, M., Dentener, F., Doherty, R. M., Faluvegi, G., Fiore, A. M., et al. (2008). A multi-model assessment of pollution transport to the Arctic. *Atmospheric Chemistry and Physics*, *8*(17), 5353–5372.
Simon, H., Beck, L., Bhave, P. V., Divita, F., Hsu, Y., Luecken, D., et al. (2010). The development and uses of EPA's SPECIATE database. *Atmospheric Pollution Research*, *1*(4), 196–206.
Simpson,I. J., Akagi, S. K., Barletta, B., Blake, N. J., Choi, Y., Diskin, G. S., et al. (2011). Boreal forest fire emissions in fresh Canadian smoke plumes: C1-C10 volatile organic compounds (VOCs), CO_2, CO, NO_2, NO, HCN and CH_3CN. *Atmospheric Chemistry and Physics*, *11*(13), 6445–6463.
Simpson, I. J., Meinardi, S., Blake, D. R., Blake, N. J., Rowland, F. S., Atlas, E., & Flocke, F. (2002). A biomass burning source of C1-C4 alkyl nitrates. *Geophysical Research Letters*, *29*(24), 2168. https://doi.org/10.1029/2002GL016290
Simpson, I. J., Sulbaek Andersen, M. P., Meinardi, S., Bruhwiler, L., Blake, N. J., Helmig, D., et al. (2012). Long-term decline of global atmospheric ethane concentrations and implications for methane. *Nature*, *488*(7412), 490–494.
Singh, H. B. (1987). Reactive nitrogen in the troposphere. *Environmental Science & Technology*, *21*(4), 320–327.
Stettler, M. E. J., Eastham, S., & Barrett, S. R. H. (2011). Air quality and public health impacts of UK airports. Part I: Emissions. *Atmospheric Environment*, *45*(31), 5415–5424.
Talbot, R. W., Dibb, J. E., Scheuer, E. M., Bradshaw, J. D., Sandholm, S. T., Singh, H. B., et al. (2000). Tropospheric reactive odd nitrogen over the South Pacific in austral springtime. *Journal of Geophysical Research*, *105*(D5), 6681–6694.
Talukdar, R. K., Burkholder, J. B., Hunter, M., Gilles, M. K., Roberts, J. M., & Ravishankara, A. R. (1997). Atmospheric fate of several alkyl nitrates part 2: UV absorption cross-sections and photodissociation quantum yields. *Journal of the Chemical Society, Faraday Transactions,93*(16), 2797–2805.
Torres, A. L., & Thompson, A. M. (1993). Nitric oxide in the equatorial Pacific boundary layer: SAGA 3 measurements. *Journal of Geophysical Research (1984-2012)*, *98*(D9), 16,949–16,954.
Travis, K. R., Jacob, D. J., Fisher, J. A., Kim, P. S., Marais, E. A., Zhu, L., et al. (2016). Why do models overestimate surface ozone in the Southeast United States? *Atmospheric Chemistry and Physics*, *16*(21), 13,561–13,577.
Turner, A. J., Jacob, D. J., Wecht, K. J., Maasakkers, J. D., Lundgren, E., Andrews, A. E., et al. (2015). Estimating global and North American methane emissions with high spatial resolution using GOSAT satellite data. *Atmospheric Chemistry and Physics*, *15*(12), 7049–7069.
Turnock, S., Wild, O., Dentener, F., Davila, Y., Emmons, L., Flemming, J., et al. (2018). The impact of future emission policies on tropospheric ozone using a parameterised approach. *Atmospheric Chemistry and Physics Discussions*, *18*, 1–41.
Tzompa-Sosa, Z. A., Mahieu, E., Franco, B., Keller, C. A., Turner, A. J., Helmig, D., et al. (2017). Revisiting global fossil fuel and biofuel emissions of ethane. *Journal of Geophysical Research: Atmospheres*, *122*, 2493–2512. https://doi.org/10.1002/2016JD025767
Valin, L. C., Russell, A. R., & Cohen, R. C. (2013). Variations of OH radical in an urban plume inferred from NO_2 column measurements. *Geophysical Research Letters*, *40*, 1856–1860. https://doi.org/10.1002/grl.50267
Vestreng, V., & Klein, H. (2002). Emission Data Reported to UNECE/EMEP: Quality assurance and trend analysis & presentation of WebDab (Tech. Rep. EMEP/MSC-W NOTE 1127 1/2002). Oslo, Norway: Norwegian Meteorological Institute.
Walker, T. W., Martin, R. V., van Donkelaar, A., Leaitch, W. R., MacDonald, A. M., Anlauf, K. G., et al. (2010). Trans-Pacific transport of reactive nitrogen and ozone to Canada during spring. *Atmospheric Chemistry and Physics*, *10*(17), 8353–8372.
Wesely, M. L. (1989). Parameterization of surface resistances to gaseous dry deposition in regional-scale numerical models. *Atmospheric Environment (1967)*, *23*(6), 1293–1304.
Williams, J. E., Le Bras, G., Kukui, A., Ziereis, H., & Brenninkmeijer, C. A. M. (2014). The impact of the chemical production of methyl nitrate from the $NO + CH_3O_2$ reaction on the global distributions of alkyl nitrates, nitrogen oxides and tropospheric ozone: A global modelling study. *Atmospheric Chemistry and Physics*, *14*(5), 2363–2382.
Wu, S., Mickley, L. J., Jacob, D. J., Logan, J. A., Yantosca, R. M., & Rind, D. (2007). Why are there large differences between models in global budgets of tropospheric ozone? *Journal of Geophysical Research*, *112*, D05302. https://doi.org/10.1029/2006JD007801
Yarwood, G., Rao, S., Yocke, M., & Whitten, G. (2005). Updates to the carbon bond chemical mechanism: CB05. Final report to the US EPA.
Zafiriou, O. C., & McFarland, M. (1981). Nitric oxide from nitrite photolysis in the central equatorial Pacific. *Journal of Geophysical Research (1984-2012)*, *86*(C4), 3173–3182.
Zhang, L., Jacob, D. J., Boersma, K. F., Jaffe, D. A., Olson, J. R., Bowman, K. W., et al. (2008). Transpacific transport of ozone pollution and the effect of recent Asian emission increases on air quality in North America: An integrated analysis using satellite, aircraft, ozonesonde, and surface observations. *Atmospheric Chemistry and Physics*, *8*(20), 6117–6136.
Zhang, L., Jacob, D. J., Kopacz, M., Henze, D. K., Singh, K., & Jaffe, D. A. (2009). Intercontinental source attribution of ozone pollution at western U.S. sites using an adjoint method. *Geophysical Research Letters*, *36*, 23073. https://doi.org/10.1029/2009GL037950
Zhang, L., Jacob, D. J., Liu, X., Logan, J. A., Chance, K., Eldering, A., & Bojkov, B. R. (2010). Intercomparison methods for satellite measurements of atmospheric composition: Application to tropospheric ozone from TES and OMI. *Atmospheric Chemistry and Physics*, *10*(10), 4725–4739.
Zhang, Q., Streets, D. G., Carmichael, G. R., He, K. B., Huo, H., Kannari, A., et al. (2009). Asian emissions in 2006 for the NASA INTEX-B mission. *Atmospheric Chemistry and Physics*, *9*(14), 5131–5153.